Challenges in Enzyme Catalysis – Photosystem II and Orotidine Decarboxylase. A Density Functional Theory Treatment

Marcus Lundberg

Stockholm University
Department of Physics
2005

Thesis for the degree of doctor in philosophy in chemical physics.
Department of Physics
Stockholm University
Sweden

© Marcus Lundberg 2005
ISBN 91–7155-057–7 pp i–viii, 1–67
Printed by Universitetsservice US-AB, Stockholm

Abstract

Possibly the most fascinating biochemical mechanism remaining to be solved is the formation of oxygen from water in photosystem II. This is a critical part of the photosynthetic reaction that makes solar energy accessible to living organisms.

The present thesis uses quantum chemistry, more specifically the density functional B3LYP, to investigate a mechanism where an oxyl radical bound to manganese is the active species in O–O bond formation. Benchmark calculations on manganese systems confirm that B3LYP can be expected to give accurate results. The effect of the self-interaction error is shown to be limited. Studies of synthetic manganese complexes support the idea of a radical mechanism. A manganese complex with an oxyl radical is active in oxygen formation while manganese-oxo complexes remain inactive. Formation of the O–O bond requires a spin transition but there should be no effect on the rate. Spin transitions are also required in many short-range electron-transfer reactions.

Investigations of the superproficient enzyme orotidine decarboxylase support a mechanism that involves an invariant network of charged amino acids, acting together with at least two mobile water molecules.

List of Papers

I. M. Lundberg and P. E. M. Siegbahn, Agreement Between Experiment and Hybrid DFT Calculations for O–H Bond Dissociation Enthalpies in Manganese Complexes, *J. Comp. Chem.* 26 **2005** 661–667.

II. M. Lundberg and P. E. M. Siegbahn, Quantifying the Effects of the Self-interaction Error in DFT – When Do the Delocalized States Appear?, *J. Chem. Phys.* **In Press**.

III. M. Lundberg and P. E. M. Siegbahn, Theoretical Investigations of Structure and Mechanism of the Oxygen-evolving Complex in PSII, *Phys. Chem. Chem. Phys.* 20 **2004** 4772–4780.

IV. P. E. M. Siegbahn and M. Lundberg, The Mechanism for Dioxygen Formation in PSII Studied by Quantum Chemical Methods, **In Manuscript**.

V. M. Lundberg, M. R. A. Blomberg, and P. E. M. Siegbahn, Modeling Water Exchange on Monomeric and Dimeric Mn Centers, *Theor. Chem. Acc.* 110 **2003** 130–143.

VI. M. Lundberg, M. R. A. Blomberg, and P. E. M. Siegbahn, Oxyl Radical Required for O–O Bond Formation in Synthetic Mn-Catalyst, *Inorg. Chem.* 43 **2004** 264–274.

VII. M. Lundberg and P. E. M. Siegbahn, Minimum Energy Spin Crossings for an O–O Bond Formation Reaction, *Chem. Phys. Lett.* 401 **2005** 347–351.

VIII. A. Bassan, T. Borowski, M. Lundberg, and P. E. M. Siegbahn, Activation of Small Molecules, **In Manuscript**.

IX. M. Lundberg and P. E. M. Siegbahn, Optimized Spin Crossings and Transition States for Short-range Electron Transfer in Transition Metal Dimers, *J. Phys. Chem. B*, **In press**.

X. M. Lundberg, M. R. A. Blomberg, and P. E. M. Siegbahn, Density Functional Models of the Mechanism for Decarboxylation in Orotidine Decarboxylase, *J. Mol. Model.* 8 **2002** 119–130.

XI. M. Lundberg, M. R. A. Blomberg, and P. E. M. Siegbahn, Developing Active Site Models of ODCase – from Large Quantum Models to a QM/MM approach, *Topics in Curr. Chem.* 238 **2004** 79–112.

Reprints are made with permission from the publishers.

Comments on my participation

As a general rule, I have performed the computational investigations and prepared the manuscripts of the papers included in the present thesis. There are three exceptions. In **Paper III**, the paragraph $S_2 \rightarrow S_3$ *involving structural rearrangements* is written by my co-author. I performed the initial exploratory investigations of the mechanism discussed in this paragraph, but did not design the model in Fig. 7. In **Paper IV**, I have been active in discussions but my final contribution is limited to a distance benchmark in the section *Computational details* and preparation of minor parts of the text. In **Paper VIII**, I have written the section *Manganese complexes that oxidize water to dioxygen*.

Preface

Formation of dioxygen in photosystem II is an intriguing biochemical reaction, but the detailed mechanism remains unknown. In the present thesis, this reaction has been investigated with the theoretical method density functional theory. The same tool has also been applied to the superproficient enzyme orotidine decarboxylase. The most important results of these investigations are summarized in the thesis itself, while full length results are available in eleven scientific papers, attached at the end.

The initial chapters provide an introduction for readers not familiar with the investigated systems and/or the employed methods. Chapter 1 mainly treats photosynthesis, explains the importance of this biological process, and outlines why it is an outstanding challenge in enzyme catalysis. Chapter 2 provides a brief background to the theoretical methods and discusses the expected accuracy of different computational approaches, with focus on the density functional B3LYP.

The first results appear in Chapter 3 that presents two investigations on the performance of B3LYP for manganese systems. One of them, described in **Paper I**, is a benchmark test of redox reactions in manganese systems. Before the release of O_2, the manganese-containing oxygen-evolving complex in photosystem II is oxidized four times by the extraction of four electrons and four protons. B3LYP performs well when the energy required to extract one electron and one proton is compared to experimental data for six synthetic manganese complexes. **Paper II** treats a basic flaw in most density functionals, the interaction of an electron with its own density. One effect of this self-interaction error is an artificial stabilization of delocalized states. Despite this, all models of the oxygen-evolving complex are correctly predicted to be localized, which is shown to be primarily due to short manganese–manganese distances.

A mechanism for oxygen evolution in photosystem II is discussed in Chapter 4 that summarizes the results in **Papers III** and **IV**. These papers analyze an oxyl radical pathway for O_2 formation and both are

inspired by a novel proposal for the structure of the oxygen-evolving complex, a Mn_3Ca-Mn cubane-like structure suggested from X-ray diffraction. In addition to the direct investigations of the mechanism for water oxidation, **Paper V** presents computational results for exchange rates of manganese ligands. This is an effort to rationalize rates of water exchange in photosystem II.

Only a few systems are capable of forming O_2 from water. The one most similar to the oxygen-evolving complex is a synthetic manganese dimer with terpyridine ligands. This biomimetic complex is discussed in Chapter 5. **Paper VI** shows that the active species in this dimer is an oxyl radical bound to manganese. Complexes with the same formal oxidation state that do not form oxyl radicals are inactive. Formation of the O–O bond requires that the system goes through a change of spin. **Paper VII** shows where this spin transition occurs for the synthetic catalyst and that it does not affect the total reaction rate. **Paper VIII** provides more examples of how biomimetic complexes can be used to understand complicated biochemical systems.

Electrons abstracted from water in the oxygen-evolving complex are parts of a chain of electron-transfer reactions that starts with the absorption of a photon. A special case of electron transfer, summarized in Chapter 6, is the short-range reaction in transition metal systems. Apart from the oxygen-evolving complex, a relevant biological example is the enzyme manganese catalase. **Paper IX** illustrates that electron transfers in antiferromagnetic systems must be accompanied by a spin transition, which leads to three alternative reaction paths.

Finally, the last chapter describes the results obtained for orotidine decarboxylase, an enzyme unique in its ability to accelerate the substrate reaction, without help from any cofactors or metal ions. Several proposals for the activity of this enzyme have been analyzed in **Paper X** and **XI**. The latter paper includes a summary of the former one, but reports novel results, mainly from a hybrid quantum mechanics/molecular mechanics approach. After these investigations, a single mechanism remains. In this mechanism, an interplay between a conserved network of charged amino acids and mobile water molecules manages to stabilize the transition state.

Contents

Preface **v**

1 Introduction **1**

2 Tools of quantum chemistry **5**
2.1 Basics of wave function methods 5
2.2 Density functional theory 8
2.3 Benchmark tests of accuracy 10
2.4 Reaction rates and transition state theory 12
2.5 Spin transitions 14

3 B3LYP applied to manganese systems **15**
3.1 Basis set selection 15
3.2 Model selection 16
3.3 Benchmark of O–H bond strengths 17
3.4 Interpreting the structures 20
3.5 Effects of the self-interaction error 21

4 Photosystem II - where plants oxidize water to oxygen **25**
4.1 Tools to investigate the reaction mechanism 27
4.2 Preliminary structures of the oxygen-evolving complex . . 28
4.3 Early S-state transitions 31
4.4 Oxyl radical and O–O bond formation 33
4.5 Water exchange 35

5 Synthetic complex for O–O bond formation from water **37**
5.1 Oxyl radical state as the active form 38
5.2 O–O bond formation 40
5.3 Spin transitions for an O–O bond formation reaction . . 42
5.4 Parallels between synthetic and biological systems 43

6 Electron transfer in transition metal dimers **45**
6.1 Antiferromagnetic dimers require spin transitions 46
6.2 Mixed-valence manganese dimers 47
6.3 Oxidation state and ligand environment 49
6.4 Ruthenium charge-transfer dimers 50

7 Orotidine decarboxylase - a superstar enzyme **51**
7.1 Concerted protonation mechanism 52
7.2 Base protonation mechanisms 55
7.3 C–C bond cleavage prior to proton donation 56

8 Concluding remarks **59**

References **61**

Acknowledgments **67**

1

Introduction

Plant photosynthesis is the biological process that has the most fundamental impact on this planet. Not only is it the dominating agent for collecting solar energy, it is also the reason there is oxygen in the atmosphere.

The first organisms that used solar energy were two different types of bacteria. However, what most people refer to as photosynthesis is the process that takes place in plants and cyanobacteria. Plant photosynthesis is a complicated process where two photosystems, I and II, work in tandem. Both are derived from systems in the early bacteria, but *photosystem II* (PSII) has incorporated a novel molecular machine, the *oxygen-evolving complex* (OEC), that uses water as reactant and releases oxygen. The protons and electrons removed from water are used in energy-conservation processes that finally lead to synthesis of carbohydrates.

O_2 is simply a by-product of the water oxidation reaction, but the impact of this by-product makes it the most important "pollutant" of all times. Prior to the evolution of photosynthetic organisms that released O_2, i.e., 2.5–3.5 billion years ago, there was no free oxygen in the atmosphere. The first hundreds of millions of years of oxygen production, this situation did not change because all oxygen reacted immediately, primarily oxidizing iron to "rust". When the reserves of metallic iron were exhausted, the amount of oxygen in the atmosphere increased "dramatically", at least on a geological timescale.

For some organisms, O_2 was toxic. But more importantly, other organisms developed ways to use oxygen as an oxidant in their metabolism, so-called aerobic metabolism. This invention was approximately 18 times more efficient than the old anaerobic way. Consequently, aerobic organisms came to dominate most biotopes while anaerobic organisms mainly thrive beneath the ground and at the

bottom of the sea. Two billion years ago, life had, thanks to photosynthesis, found ways to collect solar energy as well as ways to use it efficiently. These developments enabled the evolution of more complex forms of life.

Today, the solar energy captured by plants does no longer cover the needs of human society. Instead, more and more people rely to a large extent on the consumption of fossil fuels, the remains of photosynthetic action over millions of years. But in spite of the increasing use of energy, conversion of sunlight remains an alternative for the future. The amount of solar energy that reaches this planet is several orders of magnitude larger than the present demand. Unfortunately, most of it turns directly to heat instead of more useful forms of energy.

A possible way to develop cheap and efficient solar cells would be to learn from the process that works for plants. There are several concepts that are referred to as artificial photosynthesis, but the ultimate goal would be to use water and light as starting materials, produce hydrogen for use as fuel, and release oxygen as the only by-product. At present time, the road to practical and economical solar cells inspired by plant photosynthesis seems rather long, but understanding how plants manage to form O_2 could be an important step. However, the focus of the present thesis is on the biological system rather than the possible applications. Even if the applications are ignored, the task of understanding one of nature's greatest machines is a fantastic challenge.

Another prominent challenge when it comes to understanding enzyme activity is presented by *orotidine decarboxylase* (ODCase). Enzymes are biological machines that control and accelerate the processes of life that in many cases would take thousands of years to complete. ODCase catalyzes a step in the formation of RNA and DNA bases. Without assistance this reaction would take millions of years, but in the enzyme it takes less than a second. From the point of increasing the rate of a chemical reaction, ODCase is among the best enzymes there are. Interestingly, it works without the help of any metal ions or external organic molecules and therefore appears to be an ideal model to study "pure" enzyme catalysis. An improved understanding of how enzymes achieve their amazing catalytic power could help in designing synthetic catalysts. Solving the mechanism of a specific enzyme could assist drug development that targets diseases related to the enzyme.

The investigations of photosystem II and orotidine decarboxylase have been performed using a theoretical method called quantum chemistry. The basic idea is to apply quantum mechanics to problems in chemistry, but these theories are too complicated to be applied directly. Therefore, a number of approximative quantum chemical

methods have been developed. Still, these methods lead to complicated mathematical equations that can only be solved by computers. The method employed in the present thesis is *density functional theory* (DFT). During the last decade, the development of accurate density functional methods, like B3LYP, has made DFT a powerful tool for treating biochemical problems.

A major benefit of theoretical methods is the ability to model several hypothetical reaction mechanisms and estimate how long time they would take to complete. If a mechanism is predicted to take millions of years, it cannot be the correct enzymatic one, because those reactions are usually over in less than a second. Very often, only one modeled mechanism comes even close to the experimentally measured rate. The targets of the present investigations are to find these correct mechanisms for photosystem II and orotidine decarboxylase.

2

Tools of quantum chemistry

Quantum chemistry describes how to use quantum mechanics to solve problems in chemistry. Real chemical systems are too complicated to handle and must be reduced to simpler model systems. Still, quantum chemical methods require approximations to be able to treat even small model systems. Two conditions must therefore be fulfilled in order to get accurate results. First, the selected model should be a good representation of the chemical system of interest. At present, there is no methodological way to design a good model, and thus pragmatic approaches, based on experience, must be adopted. Second, the computational method should accurately calculate the model's properties. A more accurate method increases the reliability of the investigation, and an understanding of the possible shortcomings of a method reduces the risk of drawing incorrect conclusions from the results. To outline the expected accuracy of the present investigations, this chapter provides a brief theoretical background to quantum chemistry with focus on the method used in the thesis, density functional theory with the B3LYP functional.

2.1 Basics of wave function methods

The most important connection between a system at the quantum level and a chemical reaction observed at the macroscopic level is the energy. If energies can be calculated along a reaction pathway, this enables the prediction of reaction rates, reaction intermediates, and equilibrium constants. The energy of a system at the quantum level can, together with many other properties, be obtained by solving

the appropriate time-independent Schrödinger equation $H\Psi = E\Psi$. A branch of quantum chemistry approaches this problem directly, trying to find solutions to the Schrödinger equation, thereby getting the wave function (Ψ) and its energy eigenvalues (E). Appropriately, these are called wave function methods.[1] Another branch of quantum chemistry calculates the energy as a functional[2] of the electron density, without solving the wave function explicitly. This approach, called density functional theory, is the one employed in the present thesis. It utilizes many of the concepts developed for wave function methods and will therefore be treated in the following section.

Without further approximations, wave function methods lead to equations that cannot be solved exactly for systems beyond the H_2^+ molecule. Two common approximations are; to include a single electronic surface (adiabatic approximation) and to ignore the coupling between the movements of electrons and nuclei (Born–Oppenheimer approximation). The resulting picture is that the nuclei move on a potential energy surface created by the electrons, and minima on this surface represent stable molecules. Another common approximation is to ignore relativistic effects. They can be introduced at a later stage as perturbations.

After settling for an appropriate form of the Hamiltonian (H) in the Schrödinger equation above, approximations to the form of the wave function are introduced. Even in its simplest form, the wave function must be consistent with basic quantum mechanics like the Pauli principle. It should change sign if coordinates of two electrons are interchanged and two electrons of the same spin cannot occupy the same region in space. A simple mathematical construction that fulfills these requirements is the Slater Determinant, where each row represents an electron coordinate and each column contains a one-electron basis function.

In the Hartree–Fock (HF) approach, the shapes of the orbitals in a *single* Slater Determinant are optimized with respect to the energy, in accordance with the variational principle in quantum mechanics. The resulting molecular orbitals are linear combinations of the original one-electron basis functions. Including more basis functions in the determinant allows for a better fit to the real wave function, at the expense of an increased computational cost. With its single determinant, Hartree–Fock is the basic wave function method in quantum

[1] The present discussion of wave function methods in quantum chemistry is very brief. More details and further references can be found in general textbooks, e.g., refs [1, 2].

[2] A function uses a number as an argument and produces another number. A functional uses a function as an argument (e.g., the electron density) and produces a number (e.g., the energy).

chemistry from which more elaborate and accurate solutions can be developed.

The major issue of all quantum chemistry methods is how to handle interactions between electrons. Electrons are negatively charged and repel each other through Coulomb interactions. As discussed above, electrons of like spin cannot occupy the same region in space and therefore have a tendency to avoid each other, independent of their charges. The same-spin effect leads to longer electron–electron distances, on average, and thus lower Coulomb repulsion. This effect on the electronic energy is known as the *exchange* energy. Due to the use of an antisymmetric determinant, this interaction is well accounted for in Hartree–Fock theory.

The major problem of Hartree–Fock is that, due to the use of a single determinant, the electronic energy depends only on the interactions with the *average* electron distribution of the other orbitals. In real systems, electron movements are instantaneously correlated so that average electron–electron distances increase and the total repulsion decreases. It is customary to define the difference between the Hartree–Fock energy and the exact non-relativistic energy as the *correlation* energy. The lack of correlation energy makes Hartree–Fock a rather poor theory for evaluating relative energies of molecules.

More advanced wave function methods have ways to include electron correlation. This is usually achieved by including more determinants in the construction of the wave function. New determinants can be created by moving an electron from an occupied to a non-occupied orbital in the original determinant. These new determinants increase the flexibility of the wave function and allow electrons to correlate their movements in different orbitals. There are different ways to determine exactly how the wave function should be expanded. Prominent examples are perturbation methods, MP2 and MP4, configuration interaction (CI) and coupled cluster methods (e.g., CCSD(T)).

The different methods mentioned above all use the Hartree–Fock solution as a starting point for the wave function expansion, and therefore experience problems when a single Slater Determinant is not a good initial approximation. This happens in systems where several different electronic configurations are close in energy. Transition metal systems with their open d-shells are good examples. One solution to this problem is to use a multi-configuration method like MCSCF or CASSCF. These methods also add new determinants to the wave function but optimize their orbitals as well as the coefficients in front of them. CASPT2 additionally benefits from a perturbation treatment.

Wave function methods can reach very high accuracies. In principle, they converge to the "exact" result[3] with more determinants and more one-particle basis functions. It is therefore possible to benefit from extrapolation schemes, like G2 and G3. These methods have reached the target where they become almost as accurate as experiments (i.e., "chemical accuracy" of about 1 kcal/mol). Unfortunately, the cost of performing the calculations limits their use to rather small systems (10–20 atoms). If the target is to treat much larger systems with good accuracy, an alternative path is required.

2.2 Density functional theory

An increasingly popular way to calculate molecular properties is provided by density functional theory (DFT)[4]. In principle, DFT methods obtain their results in agreement with wave function methods, but through a different route. Although not as accurate as the best wave function methods, DFT has during the latest decade developed into a method that, for many applications, provides sufficient accuracy at a fraction of the cost of comparable wave function methods. Modeling of enzyme active sites, as performed in the present thesis, requires comparably large models, and density functional theory is therefore the best computational approach.

As the name implies, density functional theory calculates the energy of a system as a functional of the total electron density, which can be done without knowing the explicit form of the wave function. The theoretical basis of density functional theory is the observation that for non-degenerate ground states, the energy is a unique functional of the electron density $E[\rho]=E[\rho(\mathbf{r})]$ (Hohenberg–Kohn theorem) [5]. It can also be shown that the true ground state electron density minimizes the energy functional (Hohenberg–Kohn variational theorem). The second theorem proves that it is possible to calculate the energy by minimization procedures, similar to the ones used in wave function methods.

A fundamental problem in density functional theory is that the relation between energy and density, the density functional, is not known. As a starting point, it is possible to write an energy functional as a sum of terms from the nuclear potential ($v(\mathbf{r})$), kinetic energy (T) and electron–electron interactions (V_{ee}):

$$E[\rho] = \int v(\mathbf{r})\rho(\mathbf{r})d\mathbf{r} + T[\rho] + V_{ee}[\rho] \tag{2.1}$$

[3]That is, exact within the given Hamiltonian that in most cases invokes the Born–Oppenheimer approximation and neglects relativistic effects.

[4]Overviews of density functional theory are available in refs [3, 4]

An important contribution to practical density functional theory was given by Kohn and Sham when they introduced a reference system of non-interacting electrons residing in orbitals [6]. The total electron density is then obtained as a sum of each orbital squared. In theory, this density should be exact, despite the assumption of non-interacting electrons, if only the employed density functional could provide the correct electron potential. The major benefit of introducing this reference system is that large parts of the terms in eq 2.1 can be calculated exactly. If these exact parts are separated out, the previous equation can be written:

$$E[\rho] = \int v(\mathbf{r})\rho(\mathbf{r})d\mathbf{r} + T_s[\rho] + J[\rho] + (T[\rho] - T_s[\rho]) + (V_{ee}[\rho] - J[\rho]) \tag{2.2}$$

The first three terms in eq 2.2 are known. The two unknown terms, the difference in kinetic energy between the true system ($T[\rho]$) and a system of non-interacting electrons ($T_s[\rho]$), and the difference between the real electron–electron interaction ($V_{ee}[\rho]$) and the Coulomb interaction ($J[\rho]$), can be collected in a single term containing all unknowns, the so-called exchange-correlation energy $E_{xc}[\rho]$. This term is related to the correlation and exchange energies discussed for wave function methods above, but it is not exactly the same concept. If $E_{xc}[\rho]$ is introduced into eq 2.2, the functional becomes:

$$E[\rho] = \int v(\mathbf{r})\rho(\mathbf{r})d\mathbf{r} + T_s[\rho] + J[\rho] + E_{xc}[\rho] \tag{2.3}$$

Constructing a determinant of the Kohn–Sham orbitals (ϕ_i) and minimizing the total energy with respect to the shape of the orbitals leads to the following Kohn–Sham eigenvalue equation:

$$\left[v(\mathbf{r}) - \frac{1}{2}\nabla^2 + \int \frac{\rho(\mathbf{r}')}{|\mathbf{r} - \mathbf{r}'|}d\mathbf{r}' + \frac{\delta E_{xc}[\rho]}{\delta\rho(\mathbf{r})}\right]\phi_i(\mathbf{r}) = \epsilon_i\phi_i(\mathbf{r}) \tag{2.4}$$

In this equation, the analytical expressions have been introduced for the $T_s[\rho]$ and $J[\rho]$ functionals. The expression inside the brackets is the potential. It depends explicitly on the shape of the Kohn–Sham orbitals and eq 2.4 can therefore only be solved iteratively.

The computational implementations of DFT are in many aspects similar to the procedures developed for wave function methods. In its use of a single determinant and the variational principle, the Kohn–Sham approach resembles the Hartree–Fock method discussed above. A major principle difference is that the Kohn–Sham equation (eq 2.4) would give the exact energies and electron density, if the correct

exchange-correlation functional was used. The inherent accuracy of a density functional method thus depends solely on the quality of the functional.

Unfortunately, there is no systematic way to improve the exchange-correlation functionals. In spite of this, new functionals with surprising accuracy were constructed in the early 1990's, a development that made DFT a useful method for chemical applications. The reasons for the improvement of DFT functionals were the use of gradients, especially important for exchange terms, calculation of a fraction of the exchange using Hartree–Fock, and the introduction of a few empirical parameters. The most prominent functional of this generation is B3LYP, which has also been used in the present thesis. The B3LYP functional can be written:

$$F_{xc}^{B3LYP} = (1-A)F_x^{Slater} + AF_x^{HF} + BF_x^{Becke} + (1-C)F_c^{VWN} + CF_c^{LYP} \tag{2.5}$$

In this functional, as many others, contributions to the exchange-correlation functional are separated into exchange and correlation parts. F_x^{Slater} is the Slater exchange which is the solution to the exchange energy of a uniform electron gas. F_x^{HF} is the exchange part calculated with Hartree–Fock. Functionals that include this term are generally called hybrid functionals [7]. F_x^{Becke} is the gradient part of the exchange functional of Becke [8]. F_c^{VWN} is a correlation functional for the uniform electron gas constructed by Vosko, Wilk and Nusair [9]. F_c^{LYP} is the correlation functional of Lee, Yang and Parr [10]. It contains local and gradient terms and is a fit to the correlation of two electrons in a He atom. A, B, and C are the coefficients determined by Becke [11] using a fit to 116 experimental data in ref [12], where the correlation functional of Perdew and Wang [13] was used instead of F_c^{LYP} in the expression above. This led to A=0.20, B=0.72, and C=0.81. Functionals are commonly constructed to fit systems for which there exists either good experimental data or an exact solution. Density functional theory is thus semi-empirical, but still general, because once constructed, the functionals can be applied to any system.

2.3 Benchmark tests of accuracy

The preferred way to evaluate the accuracy of a theoretical method is to compare computational results with a collection of known experimental data, so-called test sets. Performances of some of the methods discussed in the previous sections are shown in Table 2.1.

Table 2.1: *Mean absolute errors in kcal/mol for selected methods in different test sets. SVWN is a combination of the functionals F_x^{Slater} and F_c^{VWN}. BLYP includes gradient contributions and is constructed from F_x^{Becke} and F_c^{LYP}. B3LYP and B3PW91 are both hybrid functionals, i.e., contains contributions from F_x^{HF}, but in B3PW91, the correlation functional is F_c^{PW91}. B98 is a ten parameter hybrid functional designed by Becke [14, 15].*

	Wave function methods				
Test set	HF	MP2	G2	G3	
G2-1[a]	74.5	7.43	-	-	
G2/97[b]	-	-	1.50	1.01[c]	
G3/99[c]	-	-	-	1.07	
	Density functionals				
Test set	SVWN	BLYP	B3LYP	B3PW91	B98
G2-1	-	4.95	2.20	-	1.75[d]
G2/97	52.40	5.77	3.31	3.65	-
G3/99	85.27	7.60	4.27	-	-

[a] Data for 55 molecules in ref [16].
[b] Data for 297 molecules in ref [17].
[d] Data for 376 molecules in ref [18].
[c] Data from ref [15].

Among the most accurate methods to date are the composite G2 [19] and G3 methods [20], and variants thereof. However, these methods are considerably more time consuming than a DFT approach. A calculation with G2MS (simplified G2 method) [21] on 20 atoms requires a computational effort comparable to a B3LYP calculation on a system of 100 atoms.

Development of density functional theory beyond B3LYP, has led to functionals that perform equally well, or in the case of B98 [14, 15], even a bit better than B3LYP. The reason to keep using B3LYP is that the expected performance of this functional is well established and areas where it fails significantly are already mapped.

The present thesis primarily concerns systems containing the transition metal manganese, but the test sets do not include any data for transition metal systems. Systematic investigations of the M–R bond strengths in small cationic systems, MR^+, where M is a first row transition metal and R is H, CH_2, CH_3 [22] or OH [23] give an average absolute error of 4.9 kcal/mol for B3LYP, and a maximum error of 9 kcal/mol. Other studies of metal–ligand bond strengths show average absolute errors for B3LYP in the range of 2–5 kcal/mol [24, 25]. Transition metal systems are notoriously difficult to treat computationally

due to the presence of nearly degenerate 3d, 4s, and even 4p levels. The relatively accurate performance of hybrid functionals like B3LYP is therefore impressive.

The three B3LYP parameters in eq 2.5 are not fitted to any transition-metal compounds. Spin splittings in iron complexes are better reproduced if the amount of Hartree–Fock exchange is decreased from 0.20 to 0.15, giving the B3LYP* functional [26, 27]. The optimal level of HF exchange does not seem to be the same for all applications [28], but investigations with B3LYP* have been included in **Papers I**, **VI**, and **VII**.

2.4 Reaction rates and transition state theory

The present thesis models the reactions in photosystem II and orotidine decarboxylase, with the goal to find the reaction mechanism, i.e., the path followed from reactant(s) to product(s). The most commonly used criteria to accept or discard a mechanism is that the calculated reaction rate should be in reasonable agreement with experimental observations.

There are two main variables that determine the reaction rate. The first one is the energy distribution of the molecules, as given by system temperature (T). The second variable is the reaction barrier ($\Delta G^{\ddagger}$), i.e., the relative free energy of the transition state (TS) connecting reactant and product, see Fig. 2.1. Quantum chemistry provides a unique way to isolate transition states and calculate transition state barriers.

The connection between temperature, barrier, and reaction rate is given by transition state theory (TST). In this theory, it is postulated that all molecules along the reaction coordinate are in thermodynamic equilibrium, which leads to the following expression for the rate (k):

$$k = \kappa \frac{k_B T}{h} e^{-\Delta G^{\ddagger}/RT} \tag{2.6}$$

where k_B is Boltzmann's constant, h is Planck's constant and κ is a probability factor that takes into account recrossings and possible tunneling effects. In general, κ is close to unity, and the effect of this variable is dwarfed by the exponential effect of the energy barrier $\Delta G^{\ddagger}$. The geometry of the transition state is optimized on the electronic energy surface, and free energy corrections are added separately by calculation of Hessian matrices. Finding the transition state on the free energy surface by a simulation technique [29], is not expected to have any significant effect on the reaction rate.

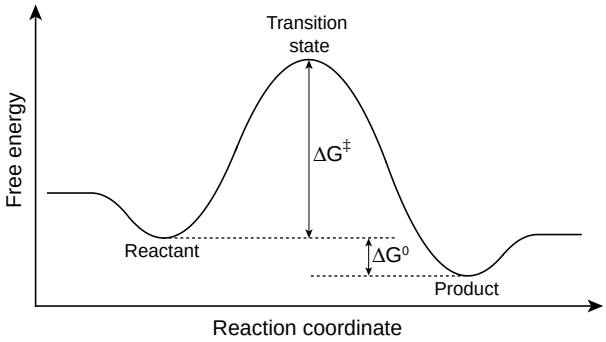

Figure 2.1: *Schematic free energy profile for a single step reaction. The barrier $\Delta G^{\ddagger}$ determines the reaction rate while ΔG^0 gives the equilibrium constant.*

The transition state barrier ($\Delta G^{\ddagger}$) is the most important property in many mechanistic investigations due to its dominating influence on the reaction rate. DFT functionals have a tendency to underestimate the barriers of several, but not all, small organic reactions [30–35]. A possible origin of this tendency is that in many DFT functionals, there remains an unphysical interaction of an electron with its own density, which leads to stabilization of states where the density is smeared out, e.g., a transition state [36]. Other potential effects of this error are discussed in section 3.5. It can simultaneously be argued that DFT could overestimate barriers of complex reactions with a high degree of multi-reference character in the transition state. How these two effects influence a particular transition state is difficult to predict, but it seems unlikely that barriers of large complicated transition states should be severely underestimated.

Most enzymes have reaction rates in the range 10–1000 s^{-1} which, according to eq 2.6, correspond to reaction barriers of 11–15 kcal/mol. In this perspective, the expected B3LYP error of 3–5 kcal/mol, as observed in benchmark tests, appears problematic. The reason why B3LYP is a useful tool for investigating enzymatic mechanisms is due to the large *difference* in barrier heights for different hypothetical mechanisms in the same enzyme. Even with an error of 3–5 kcal/mol, it is still possible to differentiate between a mechanism with a calculated barrier of 15 kcal/mol from one with a barrier of 35 kcal/mol, which is a rather common situation. However, when the predicted rate of a reaction may be wrong by 2–3 orders of magnitude, there is no hope of describing finer details of the kinetics, and factors like the transition probability, κ, can safely be ignored.

2.5 Spin transitions

A transition state can be located if reactant and product exist on the same potential energy surface, as in Fig. 2.1. **Papers VII** and **IX** treat reactions that proceed on more than one surface, because reactants and products have different total spin. For these reactions, the transition between the energy surfaces must be located, in addition to finding a possible transition state.

The largest probability for a transition between two states is encountered when the energy difference between them is small. The initial computational task is therefore to find the lowest point on the surface where the two spin states have the same energy [37–39]. This is the minimum-energy crossing point (MECP).

The rate of a transition depends both on the height of the crossing point and the transition probability. For spin transitions, the latter depends on the size of the spin-orbit coupling matrix element. This is a relativistic term, generally not included in the calculations, but possible to evaluate using a perturbation treatment. For transition metal complexes, the height of the crossing point is expected to be strongly dominating. Even a relatively poor spin-orbit coupling is not expected to slow the reaction by more than a factor of 10–100, which would correspond to an upward shift of the crossing point by approximately 2 kcal/mol. Since this is within the error bars of the B3LYP functional, the effects of spin-orbit coupling have been neglected.

3

B3LYP applied to manganese systems

Knowledge of the general accuracy of a method provides a way to estimate its performance when applied to a new problem. Another possibility is to analyze data more directly connected to the problem of interest. Since the present thesis mainly concerns manganese systems, this chapter summarizes investigations of how B3LYP performs for manganese complexes, results originally reported in **Papers I** and **II**. The chapter also contains a discussion of how modeling choices, required to treat large biochemical systems, may affect the quality of the final results.

3.1 Basis set selection

The second most important choice, after the selection of a computational method, is which basis set to use for construction of the Kohn–Sham orbitals. The shapes of the orbitals are restricted by the mathematical functions used to describe them, i.e., the *basis set*. Including more functions in the basis set usually gives a more accurate representation, but at the expense of increased computational cost.

The final energies are not very sensitive to the quality of the geometry optimization used to locate minima and transition states [40]. Consequently, geometries are optimized with a basis set of limited size, frequently the double zeta basis set lacvp. In a study of the catalytic cycle of manganese catalase, adding a polarization function to the basis set used for optimization, changes relative energies of stationary points by 0.5 kcal/mol on average [41]. At the same time, the computational cost is more than doubled.

Final energies must be calculated with a larger basis set than the one used for optimization, but the size of the basis set required to reach convergence is generally smaller for DFT than for correlated wave function methods [42]. Relative DFT energies usually converge for basis sets of triple or quadruple zeta quality (including polarization functions). In the present thesis, the most commonly used basis set is lacv3p**+, which is of triple zeta quality with a single set of polarization functions on all atoms and diffuse functions on non-hydrogens. Including a second polarization function changes relative energies in the manganese catalase cycle by 0.8 kcal/mol on average [41].

In a chemical reaction, mainly the valence electrons experience significant changes. To save computational time, the inert core electrons of manganese are, in the lacvp and lacv3p basis sets, replaced by an effective core potential (ECP) [43]. **Paper I** shows that the O–H bond strength in permanganate ($MnO_3(OH)$) changes by 2.8 kcal/mol if the all-electron 6-311+G(d,p) basis set is used instead of lacv3p**+. Using the relativistic Stuttgart/Dresden ECP instead of the non-relativistic one in lacvp changes the same bond strength by only +0.2 kcal/mol. For binding of CO to first row transition metals, relativistic effects increase the binding by 1–2 kcal/mol [44, 45], while the mean effect when switching from an ECP to an all-electron basis set is 2.5 kcal/mol [46]. However, differences of the same magnitude appear also between different all-electron basis sets. These effects illustrate the importance of the basis set for the quality of the results.

3.2 Model selection

Enzymes are built from hundreds of amino acids and therefore contain thousands of atoms, or in the case of photosystem II, around hundred thousand atoms. At present, the limit for B3LYP calculations, using the programs employed in the present thesis, Gaussian [47] and Jaguar [48] is 100–200 atoms. The major part of the enzyme must therefore be excluded from the computational model. This is only acceptable if an enzyme's activity mainly depends on the configuration close to the site where the substrates bind, the active site. In addition, the selected amino acids cannot be included in full, but this has only a minor effect on the results [41].

Excluded atoms are replaced by a homogenous medium with a dielectric constant (ϵ) of 4 to mimic the dielectric properties of the surrounding. In general, the Poisson–Boltzmann solver in Jaguar [49] has been used for solvent calculations. Relative solvent effects are generally less than 3–4 kcal/mol. Therefore, even if the errors in solvent energies are 10–30 %, the effect on relative energies is limited.

A more elaborate way to consider the surrounding protein is to include all atoms, and treat the non-reacting part with a faster but less accurate method. This approach is generally labeled QM/MM (quantum mechanics/molecular mechanics). The present thesis includes QM/MM investigations of the enzyme orotidine decarboxylase (**Paper XI**) using the program Qsite [50]. The QM part is calculated with B3LYP, the MM part with the OPLS–AA force field [51]) and the QM/MM interface is built by frozen localized molecular orbitals [52, 53]. The drawback of QM/MM methods is the increased computational effort, the questionable accuracy of the QM–MM interactions and the difficulty, due to the size of the MM part, to separate real catalytic effects from artificial ones.

3.3 Benchmark of O–H bond strengths

An important part of the present thesis concerns the mechanism for water oxidation to O_2 in photosystem II. Before the release of O_2, the manganese-containing oxygen-evolving complex in photosystem II is oxidized four times by the extraction of four electrons and four protons. This is largely equivalent to dissociating four O–H bonds. An important probe of the reaction in the oxygen-evolving complex is thus the evaluation of O–H bond strengths in manganese systems.

To validate the accuracy of the B3LYP approach, **Paper I** reports results of a benchmark of O–H bond strengths in six manganese complexes, ranging from Mn-monomers to a Mn-tetramer, see Fig. 3.1. In this test, the performance of B3LYP is satisfactory with a mean error of 3.0 kcal/mol. In addition, the performances of four other functionals are analyzed: BLYP, B3LYP* [26], B98 [14, 15], and HCTH407 [54].

Before further discussing the results of the benchmark, it should be noted that deviations between experimental and computational data have several different sources. One factor is the inherent error of the functional, the quantity of main interest in a benchmark test. Other factors are the computational approximations, i.e., the limited basis set, the use of a continuum solvent model, and neglect of relativistic effects. These approximations add error bars of 3–4 kcal/mol. There are also uncertainties in the experimental data of ±3–4 kcal/mol that partly originate from the thermodynamical cycle used to estimate the O–H bond strengths [55, 56]. The present benchmark therefore gives an indication of the accuracy of the functionals themselves, but is more appropriate as an evaluation of how well the present computational implementation treats large redox active systems.

Deviations between computed and experimental O–H bond dissociation enthalpies are shown in Fig. 3.2 and summarized in Table 3.1.

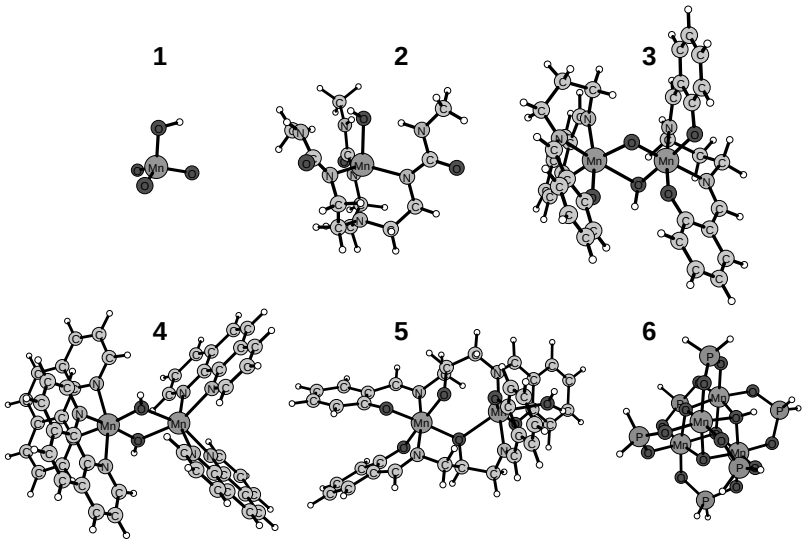

Figure 3.1: *Manganese complexes investigated in the study of ligand O–H bond strengths. The full complexes have been modeled, except for complex* **6** *where the aromatic rings of the phosphine ligands have been replaced by hydrogens.*

Complex **2** is not included in these compilations because the errors for this system are very large, tens of kcal/mol, which indicates that there is something missing in the chemical description of this complex. Ignoring Complex **2**, the B3LYP results are in general in acceptable agreement with the experimental estimates. The mean absolute deviation is 3.0 kcal/mol and the maximum error is 7 kcal/mol, see Fig. 3.2.

Treatments of transition metal systems are sensitive to the amount of Hartree–Fock exchange in the functional (see eq 2.5). Decreasing this amount from 20 % in B3LYP to 15 % in B3LYP* increases the

Table 3.1: *Mean absolute deviation (Δ) between experimental and calculated O–H bond strengths. Values are in kcal/mol. Results for complex* **2** *are not included in the calculations of the mean errors.*

	B3LYP	B3LYP*	BLYP	B98	HCTH407
Δ	3.0	5.0	18.9	3.8	9.4

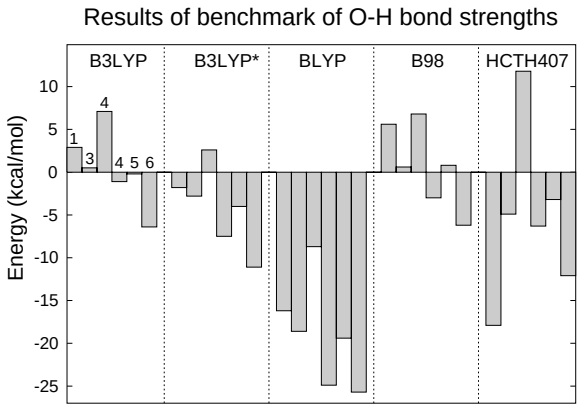

Figure 3.2: *Deviations from experimentally estimated O–H bond strengths for the five functionals B3LYP, B3LYP*, BLYP, B98, and HCTH407. For each functional the bars represent, from left to right, complex* **1** *($[MnO_3(OH)]^-$ to $[MnO_4]^-$, complex* **3** *($[Mn_2(III,IV)\text{-}\mu\text{-}O\text{-}\mu\text{-}OH]$ to $[Mn_2(IV,IV)\text{-}[\mu\text{-}O]_2]$, complex* **4** *($[Mn_2(II,III)\text{-}[\mu\text{-}OH]_2]^{+3}$ to $[Mn_2(III,III)\text{-}\mu\text{-}O\text{-}\mu\text{-}OH]^{+3}$), complex* **4** *($[Mn_2(III,III)\text{-}\mu\text{-}O\text{-}\mu\text{-}OH]^{+3}$ to $[Mn_2(III,IV)\text{-}[\mu\text{-}O]_2]^{+3}$), complex* **5** *($[Mn_2(III,IV)\text{-}H_2O]^+$ to $[Mn_2(IV,IV)\text{-}OH]^+$), and finally complex* **6** *($[Mn_4(III,III,III,IV)O_3OH]$ to $[Mn_4(III,III,IV,IV)O_4]$).*

manganese–ligand interaction which in turn weakens the O–H bond. B3LYP* therefore has a slight tendency to underestimate the bond strengths, but still performs well with a mean error of 5.0 kcal/mol. Many functionals, including B3LYP and B3LYP*, underestimate the O–H bond strength of the water molecule by 4–6 kcal/mol. The fact that O–H bond strengths of manganese ligands are too weak in the B3LYP* description, may reflect this error rather than an incorrect treatment of the transition metal system.

B98 is the only functional that performs visibly better than B3LYP in general benchmarks. In this test, B98 performs very similar to B3LYP, with a mean error of 3.8 kcal/mol. Considering modeling and experimental uncertainties, the three hybrid functionals; B3LYP, B3LYP*, and B98 must be considered equally good.

BLYP does not include any Hartree–Fock exchange. Consequently, it consistently underestimates all bond strengths and the mean absolute error is 18.9 kcal/mol. The non-hybrid functional HCTH407 performs well for some reactions but also displays large deviations, especially for permanganate, see Fig. 3.2. The mean error is 9.4 kcal/mol.

3.4 Interpreting the structures

In addition to relative energies, there are other variables that can help to discriminate between reaction mechanisms. These variables can also be used to rationalize results from a chemical perspective.

Bond lengths and angles provide valuable information concerning the nature of the system and can in many cases be compared to experimental data. Relevant examples are EXAFS investigations of the oxygen-evolving complex that give estimates of manganese–manganese distances. B3LYP performs well for bond lengths of molecules from the first and second row, with an average error of 0.013 Å [57], but Mn–Mn distances show larger errors. In a B3LYP/lacvp optimization of the synthetic Mn_4(IV,IV,IV,III)-cubane in Fig. 3.3 [58], Mn–Mn distances are on average 0.11 Å too long.

The Mulliken spin population is a tool for analyzing the electronic structure of a system. In this scheme, unpaired electrons in the total electron density are assigned to individual atoms. For high-spin manganese centers, spin populations rather well matches the number of unpaired electrons. As an example, Mn(IV) with three unpaired d-electrons gets a typical spin population of 2.8–2.9, fairly independent of the basis set.

In the present investigations of the mechanism for O_2 formation in photosystem II, it is proposed that the active species in O–O bond formation is an oxyl radical. An oxyl radical is characterized by a spin population close to 1.0, i.e., one unpaired electron on oxygen. Unfortunately, spin populations differ significantly depending on the

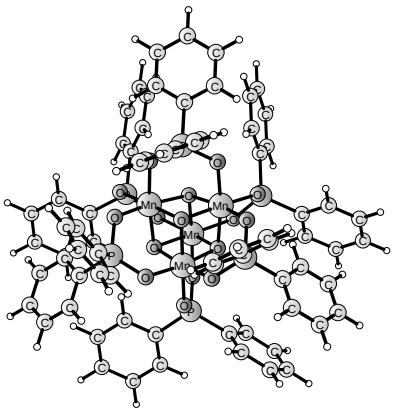

Figure 3.3: *Model of a synthetic Mn_4 cubane [58] used to test the accuracy of calculated Mn–Mn distances.*

amount of Hartree–Fock exchange in the functional as shown in **Papers I** and **VI**. For active complexes, B3LYP assigns 0.8–1.0 unpaired electrons to oxygen while the same number is <0.1 for the non-hybrid functional BLYP. In light of the superior results for hybrid functionals in the benchmark test described in section 3.3, it is reasonable to believe that B3LYP gives better spin populations.

Present DFT implementations using a single determinant cannot correctly describe open-shell low-spin states, because these states are linear combinations of different spin configurations. One example is a manganese–oxyl radical system where the spin on the radical is antiparallel to the spin on manganese. However, the energies of the correct spin states can approximately be extrapolated from high- and low-spin single determinants, using a Heisenberg–Hamiltonian and the broken symmetry approach [59].

3.5 Effects of the self-interaction error

B3LYP performs surprisingly well for a large number of transition metal applications. Still, practical DFT is inherently an approximative method and the construction of most Kohn–Sham DFT functionals leads to basic flaws. One such flaw is the non-zero interaction of an electron with its own density. In DFT, the Coulomb interaction is treated "exactly" while the exchange part is approximated. For a single electron these two terms should cancel, as they do for wave function methods like Hartree–Fock, but this is not the case for DFT. The residual interaction of the electron with itself is the self-interaction error (SIE) [60–63]. There are DFT functionals that reduce or eliminate the SIE [60, 62, 64–69] but the self-interaction corrected (SIC) functionals so far constructed, perform worse in the general benchmark tests [66, 70].

An important effect of the self-interaction error is the artificial stabilization of delocalized states [62]. An illustrative example is the one-electron system $H_2{}^+$ [71], for which the dissociation curve is shown in Fig. 3.4. B3LYP gives a qualitatively incorrect description of the dissociation process and overestimates the stability of the $H^{0.5+}$+$H^{0.5+}$ product by as much as 55 kcal/mol at infinite H–H distance.

The artificial stabilization of delocalized states is expected to be important in systems where a single electron can reside on two nearly equivalent centers. The oxygen-evolving complex with its four manganese atoms in different oxidation states is a potential candidate. Despite the self-interaction error, all calculations on that particular manganese complex correctly predict localized states. The investigations in **Paper II** illustrate that the stabilities of the localized states

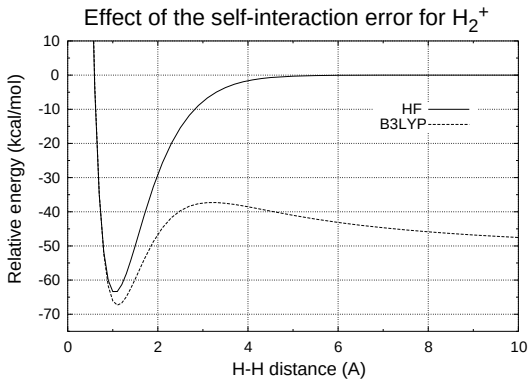

Figure 3.4: *Dissociation curves for $H_2{}^+$ calculated with Hartree–Fock (HF) and B3LYP. HF converges to the correct dissociation limit. B3LYP should converge to the same limit but, due to effects of the self-interaction error, overestimates the stability of the delocalized density $H^{0.5+}+H^{0.5+}$ at long H–H distances.*

are due to short manganese–manganese distances and relatively large reorganization energies.

It is not straightforward to calculate the magnitude of the self-interaction error. One solution is to instead estimate the energy difference between a delocalized and a localized state ($\Delta E_{loc\rightarrow del}$). A system where all the density (ρ) is located on one fragment has a larger Coulomb self-repulsion than if the density is delocalized on two equivalent non-interacting centers ($J[\rho_0] > 2*J[(\rho_0/2)] = 2*(1/2)^2 J[\rho_0] = (1/2)J[\rho_0]$).

In B3LYP, the HF exchange term cancels out some Coulomb interaction while remaining exchange terms scale as $\rho^{4/3}$. Due to the different dependence of ρ compared to the Coulomb ρ^2 term, the change in exchange energy upon delocalization is smaller than the decrease in Coulomb repulsion. This leads to an artificial stabilization of delocalized states. However, for systems with more than two atoms, the localized state is favored by an extra degree of freedom because the two fragments are free to adopt different optimal geometries. The relation between electronic and geometric effects determines whether a density will be localized or delocalized.

To quantify the effects of the self-interaction error for manganese systems, the model Mn(III,IV)-dimer in Fig. 3.5 was investigated. Mn(III,IV)-dimers have an odd electron that in the ferromagnetic state can localize on a single manganese center or delocalize to form a $Mn^{3.5+}$-$Mn^{3.5+}$-dimer. There is no direct biological precursor for this

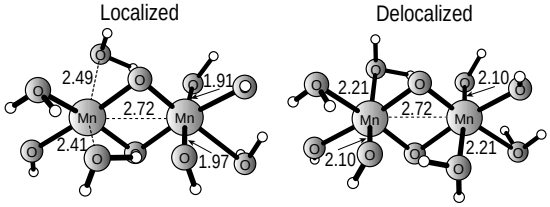

Figure 3.5: *Two states of the Mn(III,IV)-dimer $[(H_2O)_2(OH)_2Mn^{III}$-(μ-$O)_2$-$Mn^{IV}(OH)_2(H_2O)_2]^-$. The optimized state is shown to the left while the delocalized state constrained to C_i symmetry is shown to the right. Labels give distances in Å.*

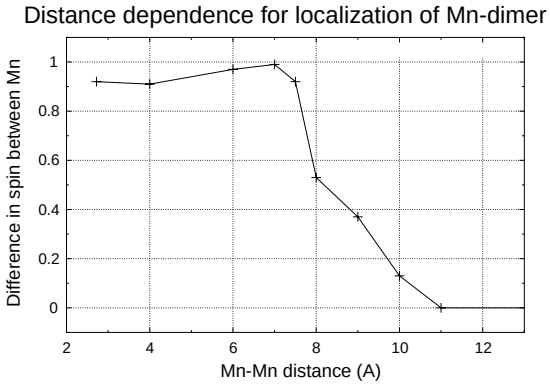

Figure 3.6: *Difference in Mulliken spin population between manganese centers in the dimer shown in Fig. 3.5 as a function of Mn-Mn distance.*

complex but a Mn(III,IV)-dimer with μ-O bridges is a basic building block of the oxygen-evolving complex in photosystem II. The results should also be applicable to a wide range of manganese complexes.

At the equilibrium Mn–Mn distance of 2.72 Å, B3LYP predicts a localized state with Mulliken spin populations of 3.82 and 2.90 for the two manganese. The energy of the unstable delocalized state can be calculated by restricting the density of the two centers to be equal (C_i symmetry). This state is unstable by 21.8 kcal/mol.

From Fig. 3.4 it is obvious that the artificial stabilization of the delocalized state increases with increasing distance between the fragments. The Mn–Mn distance is therefore stretched from 2.72 Å to 32 Å by dissociating the dimer at the metal–oxo bonds, to yield two symmetric $[(H_2O)_2(OH)_2MnO]$ fragments. Fig. 3.6 illustrates how the initially localized manganese complex gradually delocalizes as the Mn–Mn distance increases beyond 6–7 Å.

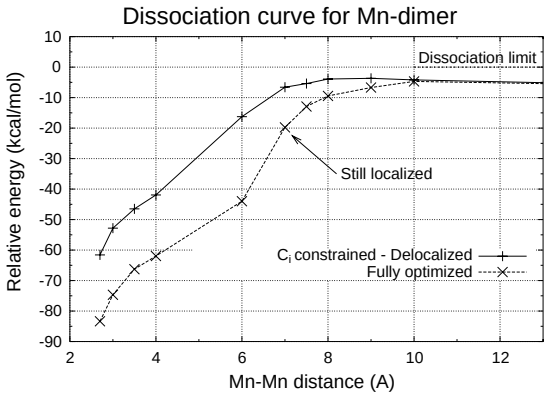

Figure 3.7: *Dissociation curves for the manganese systems shown in Fig. 3.5. Relative energies are affected by uneven changes in hydrogen bonding. At infinite Mn–Mn distances, the delocalized solution lies 10.4 kcal/mol below the dissociation limit.*

At the same time, the energy difference between the fully optimized state and the constrained delocalized state decreases. At a Mn–Mn distance of 7 Å, the localized state is stable by 13.1 kcal/mol. The energy difference decreases to 5.5 kcal/mol at 8 Å and to 0.5 kcal/mol at 10 Å. Beyond 10 Å, the fully optimized state is identical to the constrained state, see Fig. 3.7.

At infinite manganese–manganese distances, the correct dissociation limit should be the sum of the isolated Mn(III)- and Mn(IV)-complexes, but the self-interaction error artificially stabilizes a delocalized solution by 10.4 kcal/mol. An analysis of this error in terms of electronic and geometric contributions, as discussed above, shows that the electronic effect stabilizes the delocalized state by 28.2 kcal/mol, while geometry relaxation favors the localized state by 17.8 kcal/mol. The resulting error of 10.4 kcal/mol directly affects relative energies in redox reactions, ionization potentials, and electron affinities. Delocalized states also lead to erroneous descriptions of geometries and spectroscopic properties.

Fortunately, many transition metal dimers have asymmetric metal centers, short metal–metal distances, and relatively large reorganization energies, three factors that extend the stability range of the localized solution. Antiferromagnetic systems are also much less prone to delocalization. Many transition metal systems will therefore be described essentially correct.

4

Photosystem II - where plants oxidize water to oxygen

Formation of O_2 in photosystem II is one fundamental problem in biochemistry that is yet to be solved. The present investigations pursue a mechanism where an oxyl radical bound to manganese is the active species in O–O bond formation. The secret of the oxygen-evolving complex would then be to offer a route for radical formation along which the radical can be created using a limited oxidative power. When the radical has been formed, it should react with water to form O_2. Details of the oxyl radical mechanism are discussed in **Papers III** and **IV**.

The importance of photosynthetic organisms that release O_2 is discussed in Chapter 1. In total, the photosynthetic reaction involves a series of enzyme complexes. The present discussion concerns the most fascinating of these enzymes, photosystem II (PSII), and more specifically the site where water is oxidized to dioxygen, the oxygen-evolving complex (OEC). PSII is an extremely large enzyme and the OEC is only a very small part of it, see Fig. 4.1. In spite of this, the OEC is a highly complicated structure that performs a critical part of the photosynthetic reaction. Its core consists of an unprecedented four manganese atoms. All studies of manganese complexes reported in Chapter 3 have been made with this system in mind.

In photosynthetic organisms that evolve oxygen, absorption of light leads to a series of charge separations that results in a hole in the reaction center chlorophyll P680 ($P680^+$). This electron deficient species takes an electron from a nearby tyrosine residue, Tyr_Z.

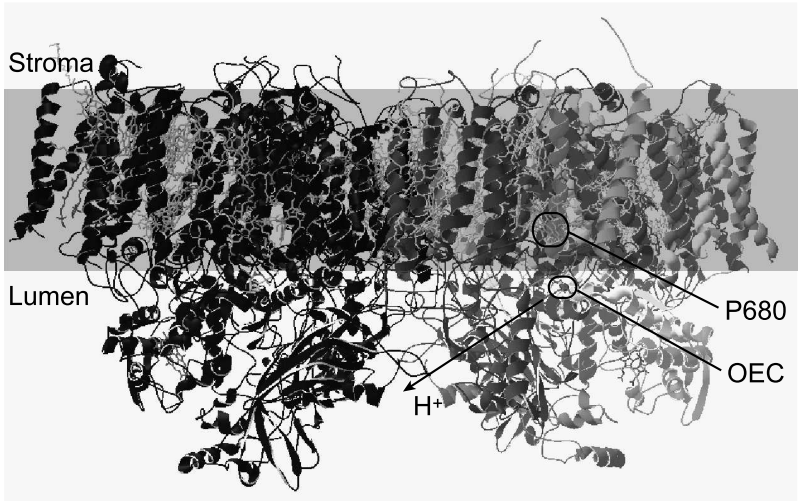

Figure 4.1: *X-ray structure of photosystem II [72] where the positions of the oxygen-evolving complex (OEC) and the reaction center chlorophyll (P680) are highlighted. PSII is a membrane protein, bound to the thylakoid membrane, as the other enzymes involved in the light-driven photosynthetic reaction. The membrane separates two aqueous phases inside the chloroplast, stroma and lumen.*

This creates a neutral tyrosyl radical, $\mathrm{Tyr}_Z\cdot$, that in a final electron-transfer step extracts an electron from the OEC. Four flashes of light recreates the $\mathrm{Tyr}_Z\cdot$ radical four times, enabling it to extract a total of four electrons. These four oxidations take the oxygen-evolving complex through five intermediate oxidation states, S_0–S_4, where the subscript denotes the number of removed electrons. Finally, the OEC releases O_2 when returning from S_4 back to S_0. A schematic illustration of the reaction is provided in Fig. 4.2, while reviews are available in refs [73, 74].

$P680^+$ is not powerful enough to abstract electrons from water and the task of the oxygen-evolving complex is to facilitate water oxidation. In addition, the OEC must enable O_2 formation, because this is required to take the cluster back to S_0, where it can go through a new reaction cycle. Even though some of the manganese centers in the oxygen-evolving complex are oxidized during the catalytic cycle, the only net reaction is water oxidation. Extracted protons and electrons are used in energy-conservation processes and O_2 is released as a by-product.

The reasons photosystem II is so challenging to describe, both experimentally and theoretically, are the complexity of the transition

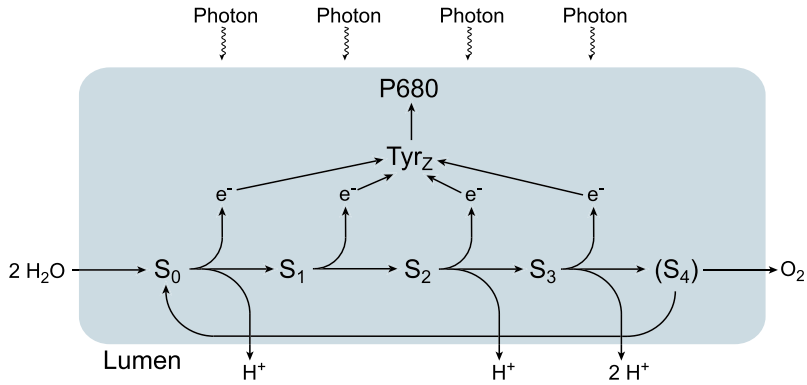

Figure 4.2: *Schematic reaction mechanism for oxygen evolution. The sequential absorption of four photons leads to the extraction of four electrons from the oxygen-evolving complex, taking it through the S-state cycle shown in the picture. S_4 has not been observed experimentally.*

metal system and the intricate flow of protons and electrons. The main advantage of theoretical methods is the relative ease with which hypothetical S-states can be isolated and evaluated. The major drawback is the requirement for an accurate model system, which can only be designed with the help from experimental data.

4.1 Tools to investigate the reaction mechanism

Most mechanistic investigations rely on the ability to calculate accurate relative energies. In the present case, this is difficult because the number of protons and electrons changes during the reaction. Investigations in refs [75, 76] and **Paper III** use the fact that the OEC is oxidized when the tyrosyl radical is reduced back to tyrosine. The power available to oxidize the oxygen-evolving complex is thus in the range of the energy required to oxidize tyrosine to a tyrosyl radical. In both systems, removal of an electron and a proton is equivalent to dissociating an O–H bond, and section 3.3 showed that B3LYP is capable of calculating O–H bond strengths in manganese systems with acceptable accuracy. In tyrosine, the bond dissociation energy is estimated to be 87 kcal/mol [77], which leads to a similar limit for oxidations of the manganese complex.

A recent X-ray structure [72] indicates that electrons and protons leave the OEC through different routes. In each transition, $\mathrm{Tyr}_Z\cdot$ thus

accepts only the electron and its redox potential may be increased by a nearby protonated histidine. This in turn increases the energy available for oxidation of the OEC by an estimated 5 kcal/mol. In addition, the flow of protons is not equally distributed over the S-state transitions, see Fig. 4.2 [78, 79]. To be able to model these transitions, proton extraction is calculated separately from electron extraction. The O–H bond energy criteria discussed above is thus divided into a proton and an electron abstraction criteria, which enables calculation of relative energies for each individual step.

Another probe of the S-state transitions is a comparison between calculated Mn–Mn and Mn–Ca distances and corresponding values given by EXAFS [80–83], keeping in mind that B3LYP seems to overestimate Mn–Mn distances by 0.11 Å on average, as shown in section 3.4.

4.2 Preliminary structures of the oxygen-evolving complex

One problem in the investigations of the OEC has been the lack of a structure. The first step toward a structure came from Zouni *et al* [84, 85], and later from Kamiya *et al* [86], whom at rather low resolution were able to suggest positions for the four manganese atoms, but without Ca or amino acid ligands. A second step was provided by Barber and Iwata *et al* [72], when they could assign a number of amino acid ligands and suggest a position for calcium inside the cluster.

Both **Papers III** and **IV** are inspired by the structural proposal in ref [72]. In this context it should be noted that the structural assignments of the three groups are not identical. All of them must be regarded as tentative, both due to the low resolution (3.2–3.5 Å) and due to the possibility that the X-ray diffraction process reduces the OEC, which could possibly lead to a loss of order. Still, the suggested structures provide interesting starting points for theoretical investigations.

However, at a stage prior to the publication of the X-ray structure by Barber and Iwata *et al*, the position of the calcium with respect to the manganese was not settled. An early interpretation of the OEC X-ray data was a cubane, with four corners occupied by manganese and oxo groups in the other four. One metal atom extends from the cubane, and this was assumed to be Ca.

The ambiguity regarding the position of Ca provided an opportunity to evaluate structural alternatives using computational methods. For this purpose, three different structures, shown in Fig. 4.3, were designed with different positions of the metal atoms within the same

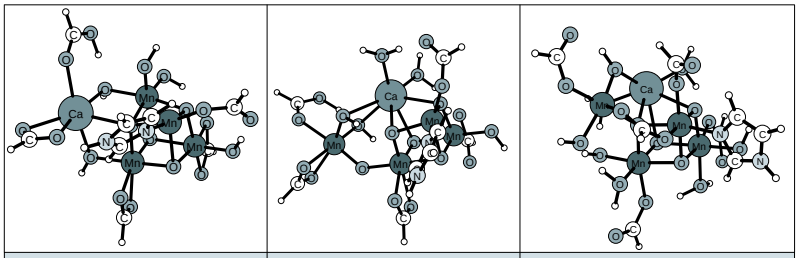

Structure **1** Mn_4-cubane - outer Ca	Structure **2** Mn_3Ca - (μ-O) - outer Mn	Structure **3** Mn_3Ca - Mn where three Mn share oxo bridge

Figure 4.3: *Selected models of the oxygen-evolving complex used in a theoretical investigation of possible structural assignments.*

Table 4.1: *Calculated Mn–Mn and Mn–Ca distances in the S_2 state for selected models of the OEC in Fig. 4.3, compared to EXAFS data. Note that B3LYP overestimates Mn–Mn distances by 0.10–0.15 Å.*

			Distances (Å)		
Model	Cubane	Outer metal	"Short" Mn–Mn	"Long" Mn–Mn	Mn–Ca
1	Mn_4	Ca	2.87, 2.88, 2.95, 2.96, 3.06, 3.07	None	3.37, 3.39
2	Mn_3Ca	Mn	2.84, 2.86, 3.01	3.33	3.27, 3.38, 3.48
3	Mn_3Ca	Mn	2.89, 2.90, 2.99,	3.49, 3.50	3.32, 3.33, 3.36, 3.40
EXAFS[a]			2.7, 2.7, 2.7	3.3	3.4, 3.4

[a] Data from refs [81, 82].

general framework. By comparing calculated metal–metal distances with those suggested by EXAFS, see Table 4.1, it is obvious that especially Model **2**, but also Model **3**, fits the experimental data significantly better than the original Mn_4-cubane suggestion (Model **1**). A Mn_3Ca-Mn model is also in much better agreement with EPR data [87, 88] and the position of Ca inside the cubane could later be supported by X-ray anomalous difference maps [72]. The final published structure of the OEC is shown in Fig. 4.4. Although it is similar to Model **3**, Model **2** may still be a valid alternative, especially in light of the uncertainties in the structural assignments.

In addition to the questions regarding the metal positions, the final X-ray structure does not assign enough ligands to fill the coordination shells of the metals. In the computational models, a re-

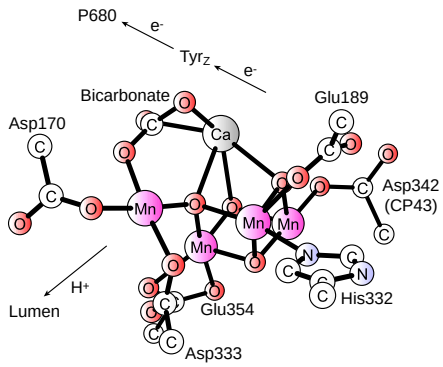

Figure 4.4: *X-ray structure of the oxygen-evolving complex with assigned amino acid ligands and a bicarbonate ligand. Hydrogen atoms are excluded from the picture. Directions for proton and electron transfer have been suggested [72].*

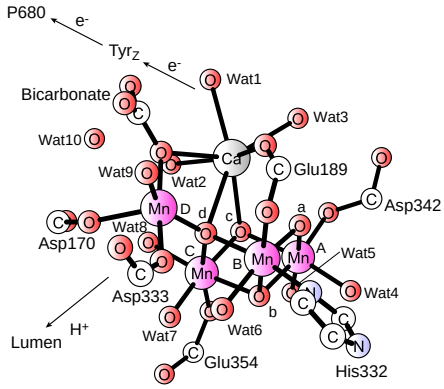

Figure 4.5: *Computational model of the structure of the oxygen-evolving complex, including ten water derived ligands added in the calculations. Hydrogen atoms are omitted for clarity. In the S_1^{-1} state, Wat4, Wat8, and Wat9 are hydroxide ligands while remaining terminal ligands are water.*

fined version of the X-ray structure has been designed by adding up to ten water-based ligands, see Fig. 4.5, and assigning protonation states to all the ligands. The choice of oxidation state follows the Mn_4(III,III,IV,IV) suggestion for the S_1 state [80, 88–90], but oxidation states of individual manganese centers, as well as changes during the S-state transitions, are proposed from computational results.

At this stage, the difference between the models in **Papers III** and **IV** can be discussed. The latter paper is a continuation of the

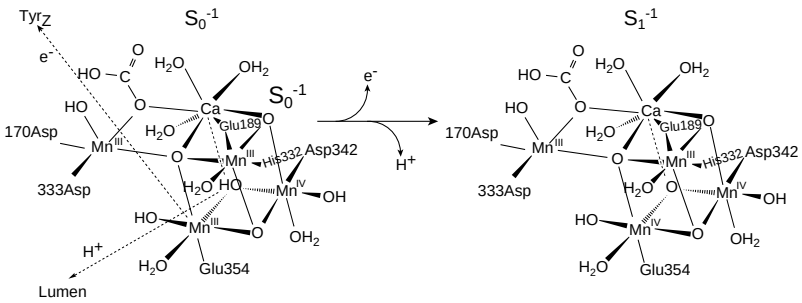

Figure 4.6: *Proposed $S_0^- \rightarrow S_1^-$ transition. Dashed arrows show the routes of the electron and the proton after leaving the oxygen-evolving complex.*

former, but uses the published X-ray structure instead of a preliminary version, which leads to some changes, e.g., in the coordination of Glu189 and Asp333. Further, it follows the X-ray structure more closely, keeps the bicarbonate and constrain amino acids by fixing terminal atoms in their X-ray positions. Despite these differences, the descriptions of the S-state transitions are stable. There is one major difference, **Paper III** follows an indirect suggestion that MnA is oxidized in the $S_1 \rightarrow S_2$ transition [91], while **Paper IV** does not. The present discussion follows the results reported in **Paper IV**, which are obtained using the model in Fig. 4.5.

4.3 Early S-state transitions

In the presently discussed model, the resting S_0 state is the S_0^{-1} state, where the subscript denotes the S-state and the superscript denotes the charge of the model. The proposed oxidation state is Mn(IV,III,III,III), counting from MnA to MnD (refer to Fig. 4.5 for atomic labels). Of the bridging ligands, only c-oxo is protonated while all terminal ligands are water, except three hydroxide ligands Wat4, Wat8, and Wat9, see Fig. 4.6.

In the first S-state transition, a proton and an electron is lost when going from S_0^{-1} to S_1^{-1}. The electron is taken from MnC in the cube and the proton from the bridging c-oxo group, see Fig. 4.6. By considering electron and proton transfers separately, an energy diagram can be designed that shows the relative energies of all the states along the reaction pathway, see Fig 4.7. In this energy diagram, the negative S_0 and S_1 states are more stable than the neutral ones, which is the basis for assigning this as an $S_0^{-1} \rightarrow S_1^{-1}$ transition rather than an $S_0^0 \rightarrow S_1^0$ transition. Further, the potential energy diagram shows that

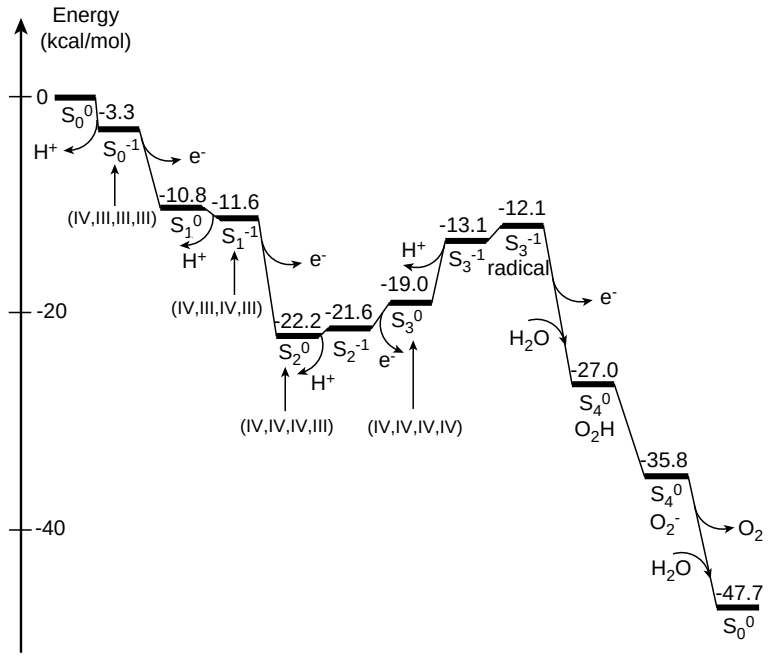

Figure 4.7: *Calculated potential energy diagram for the full S-state cycle of the oxygen-evolving complex. The energy diagram is based on calculated energies, an estimated electron affinity of 126 kcal/mol for the receiving $Tyr_Z\cdot$, and a proton affinity of the accepting lumen of 292 kcal/mol. Together, these two parameters are fitted the overall exothermicity of the reaction (approximately 47 kcal/mol), but the relation between them is chosen to get a good description of the S-state transitions.*

the transition is energetically favorable and should proceed without problems. Structurally, the transition leads to a decrease of a Mn–Mn bond length in agreement with EXAFS, although there are discrepancies when it comes to the relative lengths of the Mn–Mn distances in S_1 [81].

In the next transition, only an electron is removed from the cluster which makes it an $S_1^{-1} \rightarrow S_2^0$ transition. This is seen in Fig. 4.7 as a transition from S_1^{-1} to an S_2 state where S_2^0 is more stable than S_2^{-1}. The change in system charge is in agreement with experimental assignments [78, 79]. The electron is once again removed from a Mn(III) in the cubane, this time it is MnB, see Fig. 4.8. Note also that a proton is transferred from Wat7 to Wat8, both of them ligands to MnC.

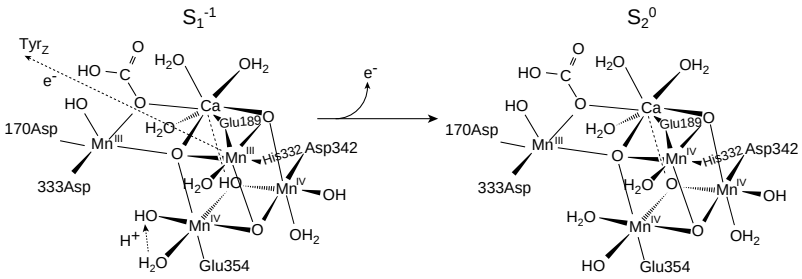

Figure 4.8: *Proposed $S_1{}^{-}\rightarrow S_2{}^{0}$ transition. One dashed arrow shows the schematic route of the electron, the other arrow illustrates a proton transfer between two ligands on MnC.*

4.4 Oxyl radical and O–O bond formation

From an energetic point of view, oxidation of Mn(III) to Mn(IV) in the early S-state transitions is generally not problematic and could, in principle, be accomplished by almost any manganese complex. However, previous DFT calculations indicate that the O–O bond is not formed with a reasonable barrier, except in mechanisms involving an oxyl radical [75, 76]. The difficult task is to find a reasonable energy for an S-state transition that leads to formation of an oxyl radical.

The $S_2\rightarrow S_3$ transition is intriguing because it is known experimentally that the structure rearranges in this step, but there is disagreement both when it comes to the nature of the rearrangement and what species is oxidized [90, 92]. The present suggestion for an $S_2^0\rightarrow S_3^0$ transition agrees with Dau *et al* [83], in that an extra short Mn–Mn distance is created. This happens when the terminal water ligand Wat8, loses one proton, transfers the second to Wat7, and becomes a bridging ligand between MnC and MnD, see Fig. 4.9. This $S_2^0\rightarrow S_3^0$ transition is almost thermoneutral (+3 kcal/mol).

However, the desired transition involves creation of an oxyl radical. A radical state can be reached by removing the proton that was donated to Wat7 in the previous transition, creating an S_3^{-1} state. In this state, the outer MnD can extract an electron from the now bridging ligand Wat8, turning it into an oxyl radical. At the same time, MnD loses its coordination to the same oxyl radical. The resulting S_3^{-1}-radical structure is shown in Fig. 4.10. It is only 1 kcal/mol less stable than the S_3^{-1} state where all manganese are Mn(IV), see Fig. 4.7.

However, compared to the S_3^0 state, and further back to S_2^0, the oxyl radical is not stable. In the present model, the total energy required to reach the oxyl radical is 10 kcal/mol, see Fig. 4.7. This leaves

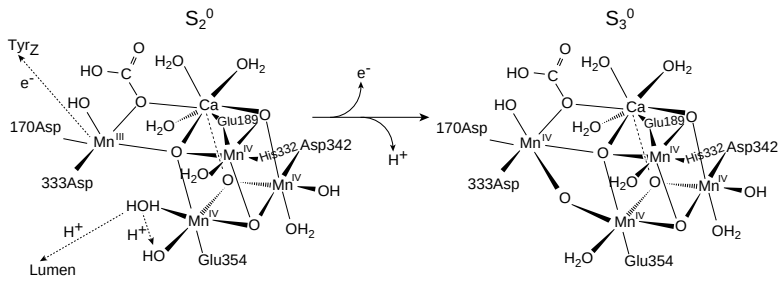

Figure 4.9: *Proposed $S_2{}^0 \rightarrow S_3{}^0$ transition. One dashed arrow shows the schematic route of the electron and two arrows show the routes of the two protons. Notice the structural change where the terminal water in S_2 becomes a bridging oxo in S_3.*

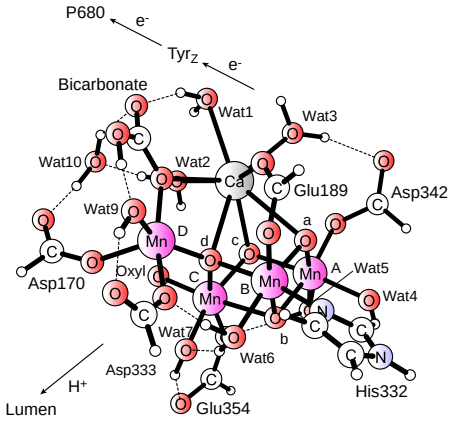

Figure 4.10: *Optimized radical S_3 state. The radical position, a little left of the center, is marked Oxyl. Dashed lines show the hydrogen bonding network.*

very little room for O–O bond formation because the entire barrier should not exceed 15 kcal/mol. Modeling O–O bond formation from the oxyl radical state gives a barrier around 17 kcal/mol, indicating that radical formation must be close to thermoneutral.

The final electron is removed during O–O bond formation and the energy decreases when the S_4^0 state is formed with MnC as a Mn(III)-peroxide. In the next step, the peroxide donates its proton to the bridging c-oxo group. Finally, the complex returns back to the S_0-state after releasing O_2 and binding a new water molecule at MnC.

In summary, the results presented here show how theoretical methods have been used to evaluate structural proposals. In addition, very reasonable S-state transitions have been proposed up to S_2, and these results can explain the uneven proton release pattern. Still, more efforts are required to find reasonable energies for the higher S-state transitions. New attempts can either use a modified ligand assignment or investigate slightly different positions of the metal atoms.

4.5 Water exchange

A large number of different experimental probes have been applied to photosystem II. One of them is the measurement of exchange rates of the two water molecules that combine to form O_2 in the $S_3 \rightarrow (S_4) \rightarrow S_0$ transition [93]. If these exchange rates could be rationalized, they would provide information on the nature of the water-based ligands and the oxidation state of the manganese center(s) that they bind to. To understand how these factors affect water exchange rates, modeling of ligand exchange in manganese systems has been performed and results are reported in **Paper V**.

In the OEC, water-based ligands (H_2O, OH^-, and O^{2-}) bind in terminal and bridging positions, see Fig. 4.5. Many of these positions are accessible in simple monomeric and dimeric models. For the manganese dimer in Fig. 4.11, a terminal water ligand exchanges with a barrier of 8.6 kcal/mol. The bridging oxo group exchanges through a ring-opening mechanism with a barrier of 19.2 kcal/mol. These numbers change by ± 3 kcal/mol depending on oxidation state, position of Ca, and the nature of the ligand trans to the exchanging ligand.

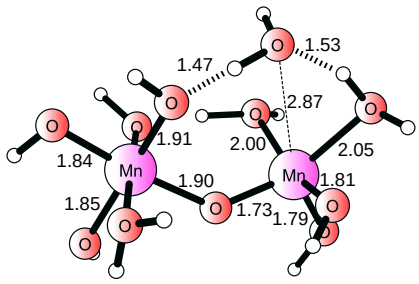

Figure 4.11: *Rate-limiting transition state for exchange of a μ-oxo group in the Mn-dimer $[(H_2O)_2(OH)_2Mn^{IV}(\mu\text{-}O)_2Mn^{IV}(H_2O)_2(OH)_2]H_2O$. The dashed line represents the reaction coordinate (formation of a bond between manganese and the incoming water ligand). Numbers represent distances in Å.*

An attempt is made to rationalize the experimental water exchange rates, using information from **Papers III** and **IV**. The conclusions are slightly different than outlined in the original paper (**Paper V**). Experimentally, one water molecule is bound already in S_0 where it exchanges with a barrier of 15.4 kcal/mol. It is here proposed to be a terminal ligand, e.g., Wat8 bound to MnC (see Fig. 4.5), despite a deviation from the estimated value for terminal hydroxo ligands on Mn(III) (10–11 kcal/mol). The discrepancy might be due to the ligand's participation in a strong hydrogen bonding network.

The ligand binds tighter after the transition to S_1 (barrier of 18.7 kcal/mol), which fits oxidation of MnC from Mn(III) to Mn(IV). Surprisingly, it binds weaker again in S_2 (barrier of 16.1 kcal/mol). A possible explanation is that the ligand accepts a proton in the $S_1 \rightarrow S_2$ transition, as suggested in Fig. 4.9. Finally, among all the changes that occur in the $S_2 \rightarrow S_3$ transition, the binding of the active water molecule does not change. This is probably not consistent with a structural change in the $S_2 \rightarrow S_3$ transition where Wat8 becomes a bridging ligand or an oxyl radical. The second water molecule exchanges faster and cannot be resolved until S_3. It is suggested that this is a water in the second shell, e.g., Wat10, that binds tighter to the cluster after the rearrangements that precede the S_3 state.

5

Synthetic complex for O–O bond formation from water

Due to the possible impact of novel renewable energy technologies, there is a search for cheap and efficient systems that can harvest solar energy in ways inspired by plants. These ambitions are still far from being realized. At present time, synthetic complexes that in some way mimic photosystem II (PSII) are not primarily precursors to large scale solar energy systems, but rather tools to improve the understanding of the reaction in the biological system.

Photosynthesis is a very complex multistep reaction and only formation of O_2 will be considered here. As no other biological systems make O_2 from water, it is natural to look for synthetic complexes that perform this task. Still, the number is limited to a few select examples, primarily containing ruthenium or manganese [94]. If the goal is to increase the understanding of O_2 evolution in PSII, the most interesting biomimetic catalyst is a manganese dimer with terpyridine ligands, shown in Fig. 5.1 [95]. In addition to its ability to form O_2, it shares some geometrical features with the OEC, both having manganese atoms linked by μ-oxo bridges. This complex has been investigated in **Papers VI** and **VII** and further discussed in **Paper VIII**.

Since only a few complexes are capable of O_2 formation, it seems reasonable that structurally related complexes perform this demanding reaction in similar ways. In Chapter 4, the active species in O–O bond formation in the oxygen-evolving complex was proposed to be a Mn(IV)-oxyl radical. If the idea of functional similarity holds, the

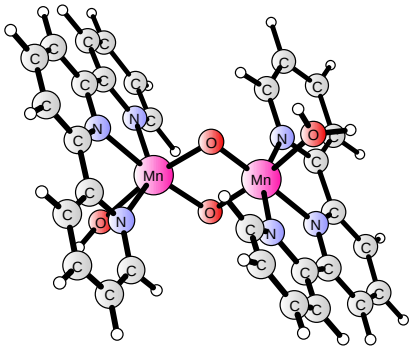

Figure 5.1: *Structure of oxygen-evolving manganese dimer [(terpy)(H_2O) Mn^{IV} (μ-O)$_2$$Mn^{III}$ (H_2O)(terpy)]$^{3+}$ (terpy=2,2′:6,2′′-Terpyridine) [95].*

active species in the synthetic complex should then also be an oxyl radical. Later, this assumption will be shown to be correct, which strengthens the case of the oxyl-radical proposal for the biological system.

The parallels between the two systems do not go beyond the O–O bond formation step. The most obvious difference is the way the active species is created. In the synthetic complex, this is accomplished by using a strong oxidant, either an oxygen atom donor like oxone (HSO_5^-) or the Ce^{3+}/Ce^{4+} redox couple [96], while the OEC manages this using only the oxidative power of the tyrosyl radical.

The original proposal from Limburg *et al* was that the active state of the synthetic complex should be the highly oxidized Mn(V)-oxo state [95]. Fig. 5.2 shows a reaction scheme for the synthetic dimer consistent with this proposal. However, there exist well characterized Mn(V)-oxo complexes that are not reactive [97–99], so the existence of a Mn(V)-state cannot be the only requirement for O–O bond formation.

5.1 Oxyl radical state as the active form

A B3LYP calculation of the formal Mn(IV,V)-oxo state of the synthetic dimer gives an electron density corresponding to a Mn(IV,IV)-oxyl radical state. The Mulliken spin populations are 2.73 and -2.73 for the two manganese centers and 0.85 for the terminal oxygen. The spin on the oxyl radical is antiparallel to the spin on the neighboring manganese. Individual manganese centers prefer high spin, in line with the manganese centers in the OEC. A state corresponding to a low-spin Mn(V)-oxo species is unstable by 12 kcal/mol.

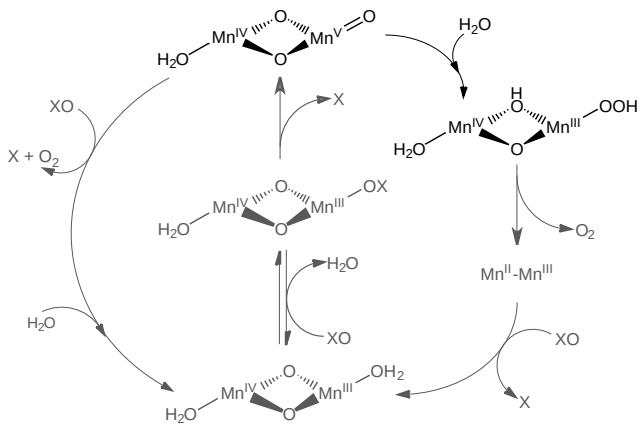

Figure 5.2: *Reaction scheme for O_2 evolution by the manganese dimer with terpyridine ligands shown in Fig. 5.1. Both water and the oxidant XO (e.g., $HSO_5{}^-$) can react with the oxidized complex to form O_2. The present theoretical study focuses on the reaction step shown in black, the O–O bond formation step with water.*

The oxyl-radical assignment is not only based on the spin population, but also on the long Mn–O distance of 1.76 Å. Mn(V)-oxo complexes have manganese–oxygen distances in the range 1.56–1.63 Å. The longer Mn–O distance in the present dimer is due to a single bond between manganese and the oxyl radical, compared to double (or triple) bonds in Mn(V)-oxo complexes.

The connection between activity and oxyl radical formation is further analyzed by looking at some Mn(V)-oxo complexes not active in O–O bond formation. Two of them have been investigated, both forming square pyramidal Mn(V)-oxo complexes in closed shell singlet states [97, 99]. The first complex has a tetraamide ligand while the second has a bis-amido bis-alkoxo ligand, see Fig. 5.3. B3LYP calculations confirm that these two complexes form singlet Mn(V)-oxo states with short Mn–O bonds around 1.56 Å. For the complex with the tetraamide ligand, a Mn(V)-oxo triplet state is found 13.1 kcal/mol above the singlet. The radical does not appear until the quintet state, but this is located 19.5 kcal/mol above the singlet. The second complex exhibits similar results.

Since the oxyl radical is predicted to be important for O–O bond formation, some tests were performed to check the sensitivity of the radical assignment. Changing the electrostatic environment by adding counter ions or optimizing in a solvent medium did not change the spin population or the manganese–oxygen distance. Improving the

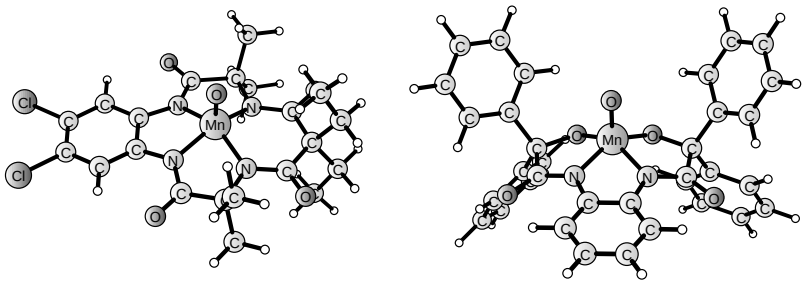

Figure 5.3: *Two formal Mn(V)-oxo complexes that are not active in O–O bond formation. Calculations predict singlet Mn(V)-oxo states, both for the complex with the tetraamide ligand (left) [97] and for the one with the bis-amido bis-alkoxo ligand (right) [99].*

basis set also had a very limited effect. The only factor that does affect the radical assignment is the choice of functional in the DFT calculation, as discussed in section 3.4. If the structure is reoptimized with the non-hybrid BLYP functional, a Mn(V)-oxo state is formed with an oxygen spin population of only -0.07 and the Mn–O distance decreases from 1.76 to 1.64 Å. However, as shown in section 3.3, the B3LYP functional is significantly better than BLYP in treating these manganese systems and the B3LYP spin assignment is therefore more likely to be correct than the BLYP one.

5.2 O–O bond formation

Once the oxyl radical is formed, either in the synthetic dimer or in the oxygen-evolving complex, it should react with a water molecule to create the O–O bond of dioxygen. To show that the radical species is an active intermediate in O_2 formation, a reasonable activation barrier ($\Delta G^{\ddagger}$) must be calculated for this reaction.

In the mechanism presented for the synthetic complex, the O–O bond is formed by approaching a water molecule toward the oxyl radical. As the reaction proceeds, the water molecule transfers a proton to a bridging μ-oxo group, see Fig. 5.4. At the same time, the manganese is reduced by accepting an electron from the oxyl radical. Since the spin on the oxyl radical is antiparallel to the spin on manganese, this will be referred to as the antiparallel pathway. The transition state is located at 23.4 kcal/mol and leads to an intermediate-spin Mn(III)-peroxide (Mulliken spin of 1.91, i.e., three spins up and one down) at 19.1 kcal/mol. The potential energy surface for this reaction step is shown in Fig. 5.5.

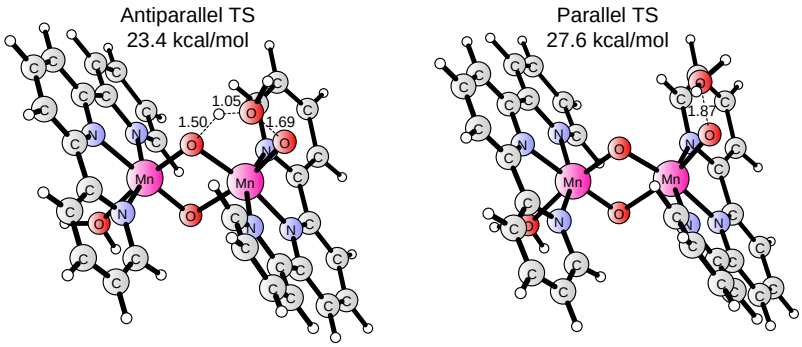

Figure 5.4: *Transition state structures for O–O bond formation in the synthetic manganese dimer. The transition state to the left corresponds to a reaction where the spin on oxygen is antiparallel to the spin on manganese. The transition state to the right corresponds to a reaction where those spins are parallel.*

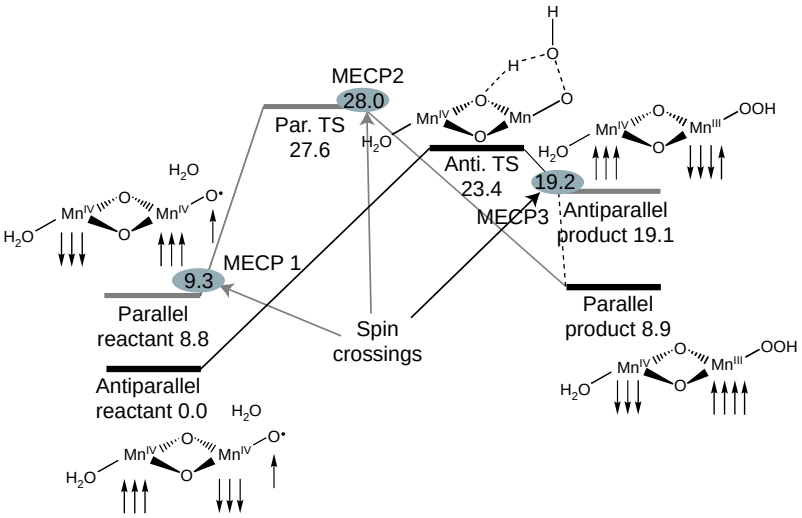

Figure 5.5: *Potential energy diagram, including spin transitions and transition states (TS), for O–O bond formation in a synthetic manganese dimer. The reaction proceeds along the reaction pathway shown in black.*

With the present ligands, the Mn(III)-product prefers a high-spin state. The reactant that is connected to the stable product is a Mn(IV)-oxyl radical where the spin on oxygen is parallel to the spin on manganese. This state lies 8.8 kcal/mol above the stable antiparallel reactant and leads to a transition state with a barrier of 27.6 kcal/mol,

see Fig. 5.5. The product is the desired high-spin Mn(III)-peroxide. As expected, this state is more stable than the intermediate-spin product, but only by 10.2 kcal/mol.

Taking both reaction pathways into account, the lowest barrier is 23.4 kcal/mol, slightly higher than the experimental upper limit of 20 kcal/mol. The deviation is within the error bars of the B3LYP method, but there could possibly be something missing in the computational description. An alternative, investigated in **Paper VII**, is that the system performs a transition between the potential energy surfaces, and in this way completes the reaction without passing any of the two transition states.

5.3 Spin transitions for an O–O bond formation reaction

In the present O–O bond formation reaction, a spin transition is required because reactant and product have different spin states. Spin transitions are important for a large number of reactions, especially those involving transition metals [100–104]. The possibility to locate these transitions [39] enables a quantitative description of their effect on reaction rates.

As shown in Fig. 5.5, there exist at least three different minimum-energy crossing points (MECPs) between the potential energy surfaces of the present redox reaction. The first crossing is located at 9.3 kcal/mol, close to the high energy reactant, see Fig. 5.5. However, if the crossing occurred at this point, the reaction would have to go through the higher of the two transition states.

The reaction thus proceeds on the antiparallel surface and crosses the transition state at 23.4 kcal/mol. There is a spin crossing in the transition state region, but this is located at 28.0 kcal/mol, above both transition states, and close to the parallel potential energy surface. The rate of spin crossing through this point is thus considerably slower than the rate of O–O bond formation on the antiparallel spin surface. Instead, as the intermediate-spin Mn(III)-product is approached on the antiparallel surface, the complex crosses over to the stable parallel spin surface. This crossing is located at 19.2 kcal/mol and is not rate limiting since the transition state itself lies at 23.4 kcal/mol.

The conclusion is that the complicated scheme of spin crossings in the manganese dimer does not affect the rate of O–O bond formation in the present system. If the mechanism for O–O bond formation is similar in the OEC, it can be expected that spin transitions have a limited effect on the reaction rate also in the biological system.

5.4 Parallels between synthetic and biological systems

The experimental results for the synthetic dimer are complicated to analyze due to the presence of reactions that compete with O–O bond formation from water [95]. The estimated 20 kcal/mol is therefore to be considered as an upper limit for the reaction barrier. One of the competing reactions is ligand exchange between the oxyl radical and solvent water. Investigations in **Paper V** give a barrier of 14.7 kcal/mol for this step.

An analysis of the data in ref [95] suggests that the barriers of the different competing reactions should not differ by more than 2–3 kcal/mol. This is consistent with the computational investigations if the barrier of the O–O bond formation step is overestimated by 3 kcal/mol, and the barrier of the exchange reaction is underestimated by the same amount. However, it is also possible that O_2 formation in the synthetic dimer occurs in a slightly different way than described above, e.g., by the participation of an additional complex as suggested in ref [96].

What does this imply for the reaction in the oxygen-evolving complex? Actually, it is not critical whether or not the presently described oxyl-radical mechanism is the best description of the reaction in the synthetic dimer. What matters is that the calculated barrier of the oxyl-radical mechanism in the synthetic dimer is 23 kcal/mol, substantially higher than the 15 kcal/mol observed for the biological system. However, this does not mean that the mechanism of the oxygen-evolving complex is different from the outlined oxyl-radical pathway. The high barrier in the synthetic dimer may instead be due to the instability of the Mn(III)-peroxide states. In the oxygen-evolving complex, both high-spin and intermediate-spin Mn(III)-states are more stable which leads to a decrease in the corresponding transition state barriers.

6

Electron transfer in transition metal dimers

Formation of O_2 is the most intriguing part of the photosynthetic mechanism. However, the reaction in photosystem II is also characterized by a large number of interesting electron-transfer steps.

As discussed in Chapter 4, the initial absorption of a photon triggers an electron to leave the reaction-center chlorophyll called P680. That electron goes through a chain of electron transfer reactions that constitutes an important part of the machinery that transfers solar energy into chemical energy. Any attempt to design systems for artificial photosynthesis requires good knowledge of the mechanisms of electron transfer, see e.g., ref [105]. The missing electron in the oxidized chlorophyll ($P680^+$) is supplied by extraction of an electron from the oxygen-evolving complex, a transfer mediated by formation of the tyrosyl radical ($Tyr_Z\cdot$). It is possible that electron transfer from the manganese cluster includes a step where the electron is first transferred to an adequate leaving position within the cluster.

In part inspired by this possibility, the present chapter describes the special case of electron transfer that can occur between transition metals in the same cluster. Two centers with different oxidation states (mixed-valence) can switch oxidation states by internal electron-transfer reactions [106]. A possible application could be molecular scale memory devices where the position of the electron in a single molecule determines the memory state [107]. Other prominent examples of mixed-valence systems are the active sites of some enzymes, e.g., the above mentioned oxygen-evolving complex in photosystem II and the Mn-dimer in manganese catalase. It has been proposed that the catalytic cycle of manganese catalase includes an

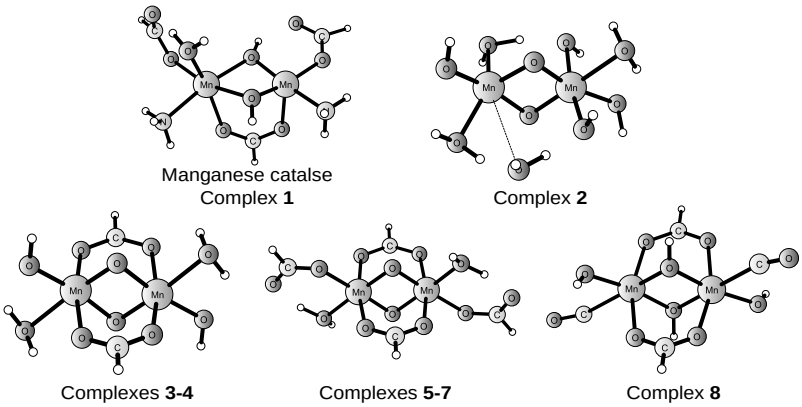

Figure 6.1: *Models of the Mn(II,III)-dimer in manganese catalase (upper left), the Mn(III,IV)-dimer discussed in the text (upper right), together with three other ligand types used to design six additional mixed-valence dimers, using different oxidation states and bridging ligands.*

electron-transfer step between the two manganese centers [108]. This step has been investigated in **Paper IX**, together with the corresponding reaction in seven other manganese dimers, all shown in Fig. 6.1.

The standard way to treat electron-transfer reactions is to estimate the reaction rate from the reorganization energy (λ) and the electron-transfer matrix element between electron donor and electron acceptor (H_{DA}), see Fig. 6.2 [109, 110]. The present investigation puts electron transfer in the same framework as other redox reactions by directly optimizing transition states of electron-transfer reactions.

6.1 Antiferromagnetic dimers require spin transitions

A twist to electron-transfer reactions in antiferromagnetic dimers with high-spin centers is the requirement for a spin transition. If an electron is transferred without changing spin, it becomes antiparallel to the electrons on the accepting metal center, which is not a stable state. A spin transition must therefore occur, but there are several options when it comes to the timing of the spin transition. This leads to at least three different electron-transfer pathways, named A, B, and C.

Route A is a single step reaction where electron transfer is concerted with the spin transition. Computationally, the transition state is the minimum-energy crossing point (MECP) between the reactant and the product state. Route B is a two-step process. The electron

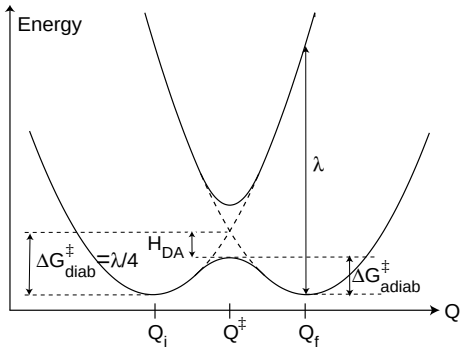

Figure 6.2: *Schematic view of a symmetric electron-transfer reaction. Q is the electron-transfer coordinate, Q^i, and Q^f represent initial (donor) and final (acceptor) states while $Q^\ddagger$ is the transition state. For a diabatic case, Marcus theory gives a barrier ($\Delta G^\ddagger_{diab}$) of $\lambda/4$. In the adiabatic case, a strong electron-transfer matrix element (H_{DA}) gives a lower barrier ($\Delta G^\ddagger_{adiab}$) and a flatter transition state region.*

first changes its spin, turning a high-spin center into one with intermediate spin. The spin of the electron that has flipped is now parallel to the spins on the second center and electron transfer will result in a stable product. The third route (C) starts with a transition from an antiferromagnetic to a ferromagnetic state. When the spins of all electrons are parallel, electron transfer can proceed in a straightforward fashion. Finally, the system relaxes back to an antiferromagnetic state.

6.2 Mixed-valence manganese dimers

To illustrate these three reaction mechanisms, this section contains results for a single mixed-valence manganese dimer. The selected system is a negatively charged Mn(III,IV)-dimer with water-based ligands, bridging μ-O and terminal OH and H_2O ligands (Complex **2** in Fig. 6.1). There exists no direct biological precursor for this model, but a Mn(III,IV)-dimer with μ-O bridges can be considered as a basic building block of the oxygen-evolving complex in photosystem II. The system was also included in the investigations of the self-interaction error in section 3.5.

In the ground state of Complex **2**, the manganese to the left has a spin of 3.82 (Mn(III), four d-electrons, high spin) while the manganese to the right has a spin of -2.81 (Mn(IV), three d-electrons, high spin). The two centers are antiferromagnetically coupled. For the concerted

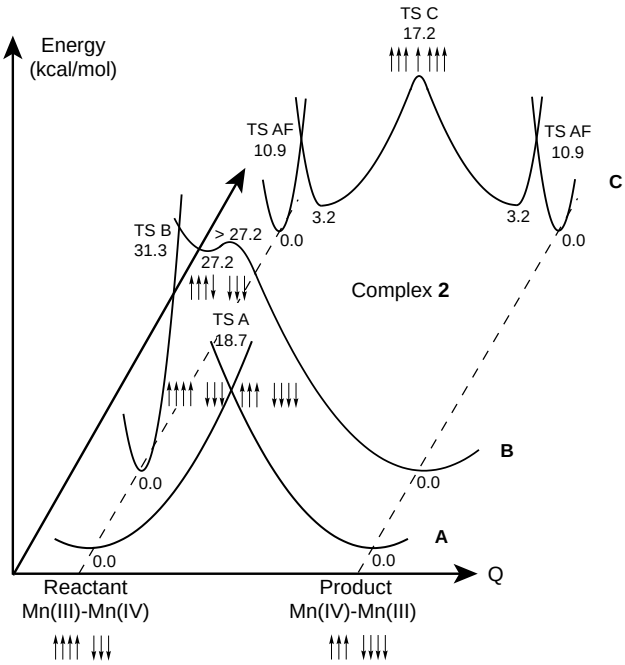

Figure 6.3: *Three potential energy diagrams for electron transfer from a Mn(III,IV)-state to a Mn(IV,III)-state in Complex* **2***,using the routes A, B, and C described in the text. The dashed lines connect the identical reactant and product states of the three reaction mechanisms.*

route A, the spin crossing between reactant and product states is located at 18.7 kcal/mol, as shown in the potential energy diagram in Fig. 6.3. Judging from the spin populations at the crossing point (3.71, -2.68), the electron fully remains on the first manganese until the spin transition occurs.

Performing the spin transition before electron transfer, according to route B, leads to spin transition at 31.3 kcal/mol above the reactant and the resulting intermediate-spin Mn(III)-state has an energy of 27.2 kcal/mol. The high energies encountered along route B show that this is not a possible pathway for electron transfer in this complex.

Continuing with route C, the transition from an antiferromagnetic to a ferromagnetic state has a barrier of 10.9 kcal/mol. From the ferromagnetic state, electron transfer proceeds with a total barrier of 17.2 kcal/mol. The barrier of the final transition back to the antiferromagnetic state is, due to symmetry reasons, identical to the barrier of the first spin transition along this route (10.9 kcal/mol).

6.3 Oxidation state and ligand environment

Two variables that affect the rates of electron transfer are oxidation state and ligand environment. Reaction barriers for the routes A–C for seven other model manganese dimers, among them a model of the active site of manganese catalase (see Fig. 6.1) are listed in Table 6.1.

The major differences between Mn(II,III)- and Mn(III,IV)-dimers are the electron-transfer matrix elements that are much smaller in the (III,IV)-complexes than in the (II,III)-complexes. This can be seen by studying the imaginary frequencies of the transition states. Small matrix elements lead to narrow transition states (see Fig. 6.2) and the (III,IV)-complexes have force constants up to 100 times larger than the (II,III)-complexes, which is reflected in imaginary frequencies in the >1000i cm^{-1} range.

Further, complexes in the (II,III)-oxidation state (**1**, **3**, **5**, and **8**) prefer the adiabatic route C over the diabatic route A by 7–12 kcal/mol. In route C, the barrier is lowered by a significant electron-transfer matrix element, while there is no such contribution for route A. This should be the major reason for the different barriers of the two routes. The spread in barrier heights between different complexes along the same route is mainly due to effects of the reorganization energy.

Complexes in the (III,IV)-oxidation state with μ-O bridges all have similar barriers for routes A and C. With the present accuracy and the neglect of the different transition probabilities for routes A and C, the preferred pathway cannot be determined.

Table 6.1: *Transition state (TS) barriers for electron transfer in the complexes* **1**-**8** *in Fig. 6.1 for the routes A and C. For route B, the energy of the intermediate-spin state is too high (25–30 kcal/mol) for this to be a viable route in any of the investigated complexes. TS AF is the barrier for a transition from an antiferromagnetic to a ferromagnetic state.*

#	Oxid. state	Bridg. ligands	TS A	TS AF	TS C	TS C freq. (cm^{-1})
			kcal/mol			
1	(II,III)	(μ-OH)$_2$	17.2	0.3	5.7	237i
2	(III,IV)	(μ-O)$_2$	18.7	10.9	17.2	1880i
3	(II,III)	(μ-OH)$_2$	22.4	2.8	13.3	335i
4	(III,IV)	(μ-O)$_2$	16.7	6.2	15.7	2740i
5	(II,III)	(μ-OH)$_2$	21.6	1.3	11.8	334i
6	(III,IV)	(μ-OH)$_2$	14.2	0.2	8.2	983i
7	(III,IV)	(μ-O)$_2$	13.0	12.4	12.8	1148i
8	(II,III)	(μ-OH)$_2$	13.6	2.3	6.4	313i

Barriers for transitions between antiferromagnetic and ferromagnetic states are largely proportional to the splitting between the states.

6.4 Ruthenium charge-transfer dimers

Attempts were made to optimize transition states for electron-transfer in two classical mixed-valence ruthenium dimers, the Creutz–Taube complex (Complex **9**) and a related dimer with a different bridging ligand (Complex **10**), see Fig. 6.4. The latter is known to be at least partly localized [111] and should have a barrier for electron-transfer.

Among the previous theoretical investigations of these two complexes, see for example refs [107, 112–115], it seems that DFT methods consistently predict complete delocalization [107, 114], which is the case also in the present study. The failures of the DFT treatment can be explained by the effects of the self-interaction error [116] discussed in section 3.5. The two charge transfer complexes have rather long Ru–Ru distances (7–12 Å), and at these distances, the artificial stabilization of delocalized states can be significant. For the present ruthenium dimers this leads to delocalized ground states from which no Ru–Ru electron transfer can take place.

The delocalized transition states encountered for the manganese dimers should also be affected by the self-interaction error but thanks to the short Mn–Mn distances (2.7–3.0 Å), the effect should be limited, maybe below 1 kcal/mol. Unfortunately, many interesting metalloorganic complexes have long metal–metal distances and therefore require alternative DFT functionals. A possible solution is to increase the amount of Hartree–Fock exchange in the functional with increasing distance between centers.

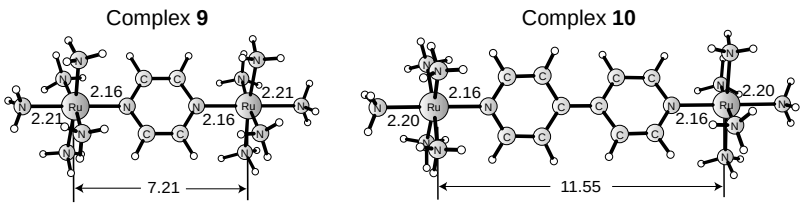

Figure 6.4: *Optimized geometries for the two Ru-dimers, the Creutz–Taube complex [decaammine(μ-pyrazine)diruthenium]$^{5+}$ (left) and the related [decaammine(μ-4,4′-bipyridine)diruthenium]$^{5+}$ (right). B3LYP predicts no barriers for electron transfer and spin populations of (0.66, 0.66) for Complex* **9** *and (0.54, 0.54) for Complex* **10**.

7

Orotidine decarboxylase - a superstar enzyme

Enzymes catalyze many reactions far better than man-made catalysts. One goal of theoretical studies of enzymes is to understand how they achieve their amazing catalytic power. In this respect, orotidine 5'-monophosphate decarboxylase (ODCase) is one of the most fascinating enzymes. The reaction barrier for decarboxylation of its substrate orotidine 5'-monophosphate (OMP), see Fig. 7.1, is 15 kcal/mol. In solution, the corresponding barrier is 38 kcal/mol. Consequently, the enzyme manages to lower the barrier by 23 kcal/mol. This rate acceleration is matched by few other enzymes [117] and ODCase performs that task without help from metal ions or organic cofactors.

Analyzing the mechanism of ODCase can therefore be an important step in understanding enzyme catalysis on a general level. It can also shed light on the requirements of computational models applied to enzymes. Results of the present investigations have originally been reported in **Papers X** and **XI**.

One main event of the substrate reaction in ODCase is that the carboxylate group attached to the pyrimidine ring leaves to form carbon dioxide (see Fig. 7.1). During this reaction, the negative charge of the carboxylate is transferred to the pyrimidine ring. In other known decarboxylations, this charge is stabilized by delocalization, either into a π-system or by a cofactor present at the active site, but this is not the case in ODCase. The other main event of the substrate reaction is that a proton replaces the carboxylate on C6 of the pyrimidine ring (refer to Fig. 7.1 for atomic labels). This proton can approach the substrate either before, during, or after the C–C bond is cleaved. These three alternatives give rise to three different classes of reaction

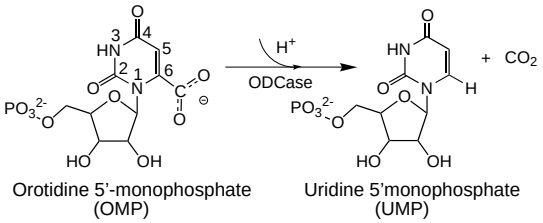

Figure 7.1: *General scheme of the substrate reaction in ODCase. Labels refer to positions in the pyrimidine ring and are used frequently throughout the text.*

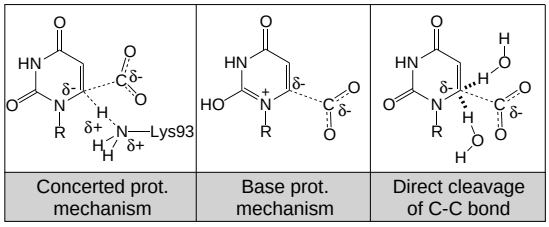

Figure 7.2: *Schematic illustration of the three reaction mechanisms treated in the present chapter. The base protonation mechanism includes protonation of O2 as well as all other sites of the pyrimidine ring.*

mechanisms (see Fig. 7.2), each discussed in separate sections below.

The conclusion from **Papers X** and **XI** is a tentative support for direct C–C bond cleavage, originally proposed by Warshel *et al* [118]. In this mechanism, stabilization of the negative charge on C6 in part comes from loosely bound water molecules that approach C6 during the reaction. In **Paper XI**, this mechanism showed promising results, but only with severe constraints of the active site or with an elaborate QM/MM treatment. Unpublished results show that the stabilization of the transition state remains if the constraints are released and the structure kept at the same local minimum. Contributions from a QM/MM treatment are not significant for well-balanced models, but become important when a smaller QM model cannot describe the changes in hydrogen bonds that occur during the reaction.

7.1 Concerted protonation mechanism

From the X-ray structure of ODCase shown in Fig. 7.3, it is expected that a lysine residue (Lys93) should be particularly important for catalysis because it seems to interact directly with the leaving

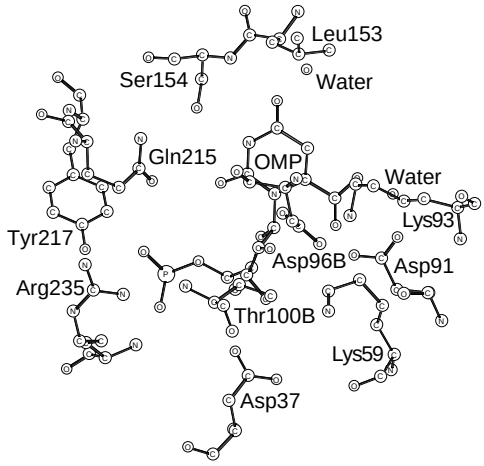

Figure 7.3: *Selected amino acids from the X-ray structure of ODCase [122].*

carboxylate [119–122]. One possibility for decarboxylation is a single step reaction where Lys93 protonates C6, concerted with cleavage of the bond between C6 and the carboxylate. In this mechanism, the negative charge developing on the ring is directly stabilized by the positive lysine.

In a model including only substrate and Lys93, see Fig. 7.4, the barrier for the concerted mechanism is 37 kcal/mol, more than 20 kcal/mol higher than the enzymatic barrier. Lys93 is part of an invariant network of charged amino acids (Lys59, Asp91, Lys93, and Asp96B) that from mutation experiments are known to be very important for the enzymatic reaction [123]. If the other three invariant amino acids of this network are included in the model, the barrier is largely unaffected (34 kcal/mol). In fact, the barrier is almost invariant to the selection of amino acids at the active site. Any effect on the interaction between the positive lysine and the carboxylate in the reactant seems to have a similar effect on the ability of lysine to donate a proton in the transition state.

Since the selected amino acids did not provide any catalytic effect, the rest of the protein matrix was included in a QM/MM description. A QM/MM treatment is expected to handle both strain and long-range electrostatic effects.

The large QM/MM model in Fig. 7.4 includes over 100 QM atoms and more than 4600 MM atoms but in spite of the size of the model, there was no sign of any important enzymatic effect. The barrier

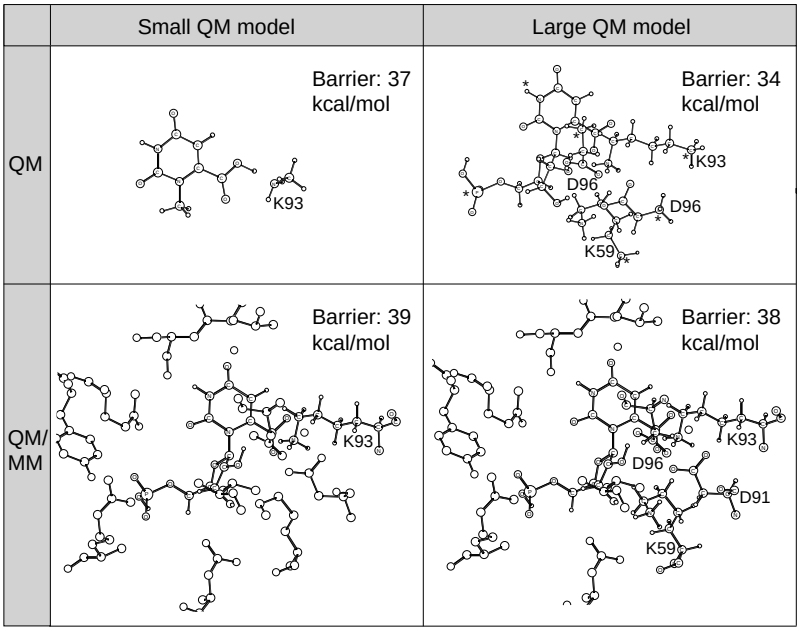

Figure 7.4: *QM and QM/MM models used to investigate the concerted reaction mechanism. For the QM/MM models, labeled atoms are included in the QM description. Hydrogen atoms in QM residues are not labeled and hydrogen atoms in MM residues are not displayed. The picture does not display all residues that are included in the MM part.*

actually increased by 2–4 kcal/mol when going from QM to QM/MM models. Although the MM energies are not as accurate as the QM energies, it would be an unlikely coincidence if errors in the QM/MM treatment masked a real protein effect.

Claims by Raugei *et al* [124] that a concerted mechanism does provide the required transition state stabilization could not be confirmed. Geometries from Car–Parrinello/molecular mechanics simulations were kindly supplied by Dr Raugei. Calculations on a model similar to the large QM model in Fig. 7.4, but including also the invariant Gln215 and Arg235, give a barrier of 42 kcal/mol. This value does not change significantly if the structures are re-optimized using B3LYP.

The reason for the discrepancy between the present results and those of Raugei *et al* is not well established. The BLYP functional used by Raugei *et al* give barriers 7 kcal/mol lower than B3LYP, but this difference cannot alone explain the discrepancies of approximately 20 kcal/mol.

7.2 Base protonation mechanisms

It is known that protonation of the pyrimidine ring leads to a significant decrease in the strength of the C–C bond [125], but it has not yet been shown that protonation can occur with a reasonable energy. The sum of the energies required to protonate the ring and break the C–C bond must not exceed the reaction barrier of 15 kcal/mol.

For this mechanism, the selection of amino acids has a significant influence on the barrier. In the initial QM study in **Paper X**, the lowest barrier is obtained for protonation of the carbonyl oxygen O2 using a model that includes all four charged amino acids close to the carboxylate (Lys59, Asp91, Lys93 and Asp96B) and Gln215 at O2. Compared to the carboxylate, the cost to protonate O2 is 7 kcal/mol, and from this protonated structure there is a 19 kcal/mol barrier for decarboxylation since the charged network stabilizes C–C bond cleavage by approximately 8 kcal/mol. The problem of that model is that the estimated protonation cost is not saturated with respect to the number of included amino acids.

To improve the modeling of relative proton affinities, two QM/MM extensions were made, see Fig. 7.5. As a comparison, two pure QM models were designed with the same QM residues as the QM/MM models. The QM/MM models give different proton affinities than the corresponding QM models but also different results between themselves, depending on whether the protonated site interacts with a QM or an MM residue, see Table 7.1.

Remembering that protonation costs of the pyrimidine ring are calculated against the site with the highest proton affinity, i.e., the

Table 7.1: *Proton affinities (kcal/mol) of different positions in the pyrimidine ring. Refer to Fig. 7.1 for labels. QM/MM models are shown in Fig. 7.5 while the QM models include only the QM residues of the QM/MM models. Values in parenthesis include large basis set effects and solvent corrections, other values are taken directly from small basis set calculations.*

	Atom label				
Model	O2	N3	O4	C5	Carboxyl.
Substrate only	280 (261)	262 (247)	293 (274)	288 (263)	324 (290)
Small QM	281 (268)	244 (242)	270 (269)	264 (259)	278 (279)
Large QM	279 (266)	245 (241)	250 (258)	253 (250)	267 (272)
Small QM/MM	295	271	299	301	317
Large QM/MM	277	254	284	284	321

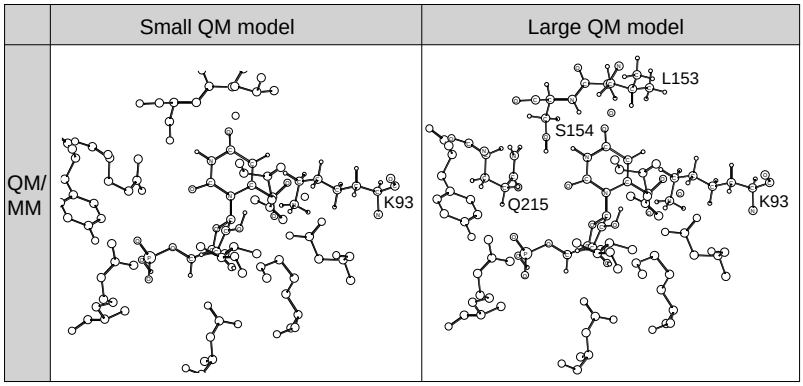

Figure 7.5: *QM/MM models used to calculate proton affinities of the pyrimidine ring. Labeled atoms are included in the QM description. Hydrogen atoms in QM residues are not labeled and hydrogen atoms in MM residues are not displayed. The picture does not display all residues that are included in the MM part.*

carboxylate group, the lowest protonation cost (6 kcal/mol) is obtained for O2 in the large QM model. This estimate is probably too low because the large QM model lacks Asp91 and Asp96B, that in other models increase the protonation cost of O2 relative to the carboxylate by 12 kcal/mol. If they were included, this would give a total protonation cost of 18 kcal/mol. Together with an estimated 19 kcal/mol required to cleave the C–C bond from previous calculations, the total barrier is 37 kcal/mol. In the QM/MM models, the lowest protonation cost is 16 kcal/mol for C5 in the small QM/MM model (see Table 7.1). Due to the high costs of protonating the substrate, the base protonation mechanism is not supported.

7.3 C–C bond cleavage prior to proton donation

The third investigated alternative is a stepwise mechanism in which the C–C bond is cleaved prior to protonation of C6, originally proposed by Warshel *et al* [118]. The simulation structures from that study were kindly supplied by Dr Strâjbl and they have been used as starting points for regular QM modeling. To keep the overall geometries close to the starting structures, several atoms had to be frozen during the optimizations, as indicated in Fig. 7.6. In these structures, the relative energy between reactant and an intermediate with a bro-

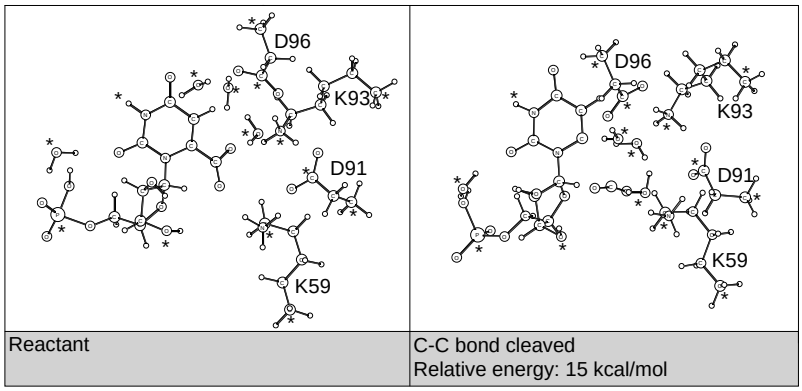

Figure 7.6: *Reactant and intermediate structures for a stepwise mechanism where the C–C bond is cleaved prior to protonation of C6. Atoms marked with asterisks (*) are kept frozen in the positions they had in the structures obtained from molecular dynamics simulations in ref [118].*

ken C–C bond is only 15 kcal/mol (thermal and entropy effects not included). This is a remarkable decrease from the high barriers of the previous mechanisms. The geometry of the transition state, with water molecules interacting with C6, indicates that these water molecules provide an essential part of the stabilization of the negative charge developing on C6. The second part of the stabilization is provided by the network of charged amino acid residues.

However, if the structures are released, this leads to large movements of amino acids and water molecules, and the apparent stabilization disappears. To avoid these rearrangements, a large QM/MM model was designed. Starting from a re-optimized reactant structure, the energy required to reach the transition state by increasing the C–C bond length is 22 kcal/mol and two water molecules find their ways to C6 without any constraints. Adding thermal corrections of -3 kcal/mol, from smaller models of the decarboxylation reaction, gives a barrier around 19 kcal/mol, still not including solvent effects. This is in reasonable agreement with the experimental barrier of 15 kcal/mol.

The modeling philosophy of the present thesis is that important energetic effects should be accessible through QM models. To handle the mobile residues, a very large QM model was designed where many hydrogen bonds are saturated and where hydrophobic residues constrain the flexibility of the active site, see Fig. 7.7.

Starting from the simulation geometries for reactant and transition state, initial calculations where the positions of all waters are

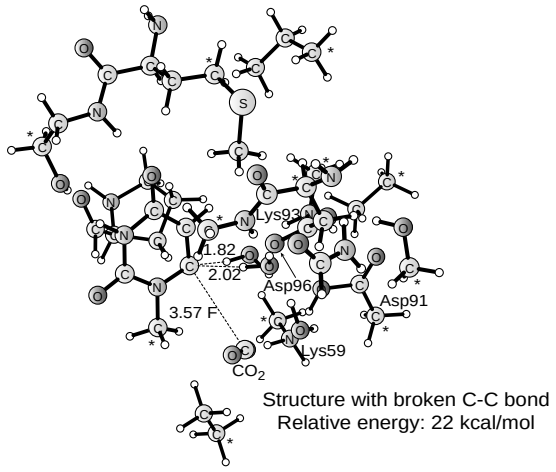

Figure 7.7: *Transition state for the large QM model gradually released from the simulation structure in ref [118]. The reaction barrier of 22 kcal/mol is calculated for the structure with a C–C bond distance of 3.57 Å. The final set of frozen atoms are marked with an asterisk (*).*

frozen, as well as two sites on each amino acid, give a relative energy of 16 kcal/mol for the structure with the broken C–C bond (bond length of 3.57 Å). These energies include corrections for solvent and thermal effects. Gradually releasing the constraints until only the terminal ends of the amino acids are frozen, increases the energy to 22 kcal/mol, but the major part of the catalytic effect still remains. Two water molecules stay in positions where they stabilize the negative charge developing on C6. A similar barrier for decarboxylation can be obtained by extending the C–C bond from the reactant structure. However, releasing the C–C bond in the transition state leads to a new minimum with a lower energy. The designed model is therefore still not stable in all details.

A value of 22 kcal/mol for the reaction barrier is too high compared to experiment but still more reasonable than for any previous mechanism. The interpretation is that the catalytic mechanism can be basically correct but missing some details. The importance of the mobile water residues and the charged network is probably the source of the difficulties in describing the mechanism of ODCase. The interactions between these groups are strong and the energy of different conformations must be reproduced accurately. In a truncated model with unsaturated hydrogen bonds, this is very difficult to achieve.

8

Concluding remarks

The investigations in the present thesis outline a radical mechanism for oxygen evolution in photosystem II. The factors enabling these investigations have not only been improvement of computational facilities, but also experimental investigations of the oxygen-evolving complex and synthesis of biomimetic complexes. The major refinements of the theoretical description in the near future will more likely be due to experimental information of higher resolution and accuracy than improved computational methods or resources. The most important development would be a confirmation of the structure of the OEC. Theoretical methods will remain unique in their "accessibility" to the highly oxidized states, which provides an opportunity to outline a detailed mechanism for O–O bond formation.

Functional mimics of the oxygen-evolving complex are mainly of use as models to increase the understanding of the natural system. There is still a long way to go before they can be used as economical systems for solar energy collection. To develop efficient solar cells, it is not enough to mimic the function of photosynthesis, because the target must be a significantly higher efficiency in harvesting solar energy compared to the process in plants.

The number of systems accessible to computational chemistry, as well as the the maximum size of these systems, is bound to increase. With improved computational resources, a limiting factor will be the time required to analyze results of calculations on bigger and bigger systems. This increases the risk of drawing incorrect conclusions from undetected artifacts. On the other hand, improved experience of modeling complicated biochemical systems will lead to increasing consensus of how enzymes achieve their catalytic powers, and which methods to use when addressing these problems.

References

[1] Szabo, A.; Ostlund, N. S. *Modern Quantum Chemistry;* Dover Publications: New York, 1989.

[2] Jensen, F. *Computational Chemistry;* Wiley: Chichister, 1999.

[3] Parr, R. G.; Yang, W. *Density-Functional Theory of Atoms and Molecules;* Oxford University Press: New York, 1989.

[4] Koch, W.; Holthausen, M. C. *A Chemist's Guide to Density Functional Theory;* Wiley: Weinheim, 2000.

[5] Hohenberg, P.; Kohn, W. *Phys. Rev. B* **1964**, *136*, 864–871.

[6] Kohn, W.; Sham, L. J. *Phys. Rev. A* **1965**, *136*, 1133–1138.

[7] Becke, A. D. *J. Chem. Phys.* **1993**, *98*, 1372–1377.

[8] Becke, A. D. *Phys. Rev. A* **1988**, *38*, 3098–3100.

[9] Vosko, S. H.; Wilk, L.; Nusair, M. *Can. J. Phys.* **1980**, *58*, 1200–1211.

[10] Lee, C.; Yang, W.; Parr, R. G. *Phys. Rev. B* **1988**, *37*, 785–789.

[11] Becke, A. D. *J. Chem. Phys.* **1993**, *98*, 5648–5652.

[12] Gill, P. M. W.; Johnson, B. G.; Pople, J. A.; Frisch, M. J. *Int. J. Quantum Chem. Quant. Chem. Symp.* **1992**, *26*, 319–331.

[13] Perdew, J. P.; Wang, Y. *Phys. Rev. B* **1992**, *45*, 13244–13249.

[14] Becke, A. D. *J. Chem. Phys.* **1997**, *107*, 8554–8560.

[15] Schmider, H. L.; Becke, A. D. *J. Chem. Phys.* **1998**, *108*, 9624–9631.

[16] Bauschlicher, C. W. J. *Chem. Phys. Lett.* **1995**, *246*, 40–44.

[17] Curtiss, L. A.; Raghavachari, K.; Redfern, P. C.; Pople, J. A. *J. Chem. Phys.* **1998**, *109*, 42–55.

[18] Curtiss, L. A.; Raghavachari, K.; Redfern, P. C.; Pople, J. A. *J. Chem. Phys.* **2000**, *112*, 7374–7383.

[19] Curtiss, L. A.; Raghavachari, K.; Trucks, G. W.; Pople, J. A. *J. Chem. Phys.* **1991**, *94*, 7221–7230.

[20] Curtiss, L. A.; Raghavachari, K.; Redfern, P. C.; V., R.; Pople, J. A. *J. Chem. Phys.* **1998**, *109*, 7764–7776.

[21] Froese, R. D. J.; Humbel, S.; Svensson, M.; Morokuma, K. *J. Phys. Chem. A* **1997**, *101*, 227–233.

[22] Blomberg, M. R. A.; Siegbahn, P. E. M.; Svensson, M. *J. Chem. Phys.* **1996**, *104*, 9546–9554.

[23] Ricca, A.; Bauschlicher, C. W. J. *J. Phys. Chem. A* **1997**, *101*, 8949–8955.

[24] Ricca, A.; Bauschlicher, C. W. J. *J. Phys. Chem.* **1994**, *98*, 12899–12903.

[25] Koch, W.; Hertwig, R. H. In *Encyclopedia of Computational Chemistry*; Schleyer, P. v. R., Ed.; Wiley: Chichester, 1998.

[26] Reiher, M.; Salomon, O.; Hess, B. A. *Theor. Chem. Acc.* **2001**, *107*, 48–55.

[27] Salomon, O.; Reiher, M.; Hess, B. A. *J. Chem. Phys.* **2002**, *117*, 4729–4737.

[28] Harvey, J. N. *Struct. Bonding* **2004**, *112*, 151–183.

[29] Truhlar, D. G.; Garret, B. C.; Klippenstein, S. J. *J. Phys. Chem.* **1996**, *100*, 12771–12800.

[30] Durant, J. L. *Chem. Phys. Lett.* **1996**, *256*, 595–602.

[31] Jursic, B. S. *Chem. Phys. Lett.* **1996**, *256*, 603–608.

[32] Glukhovtsev, M. N.; Bach, R. D.; Radom, L. *Chem. Phys. Lett.* **1996**, *260*, 558–564.

[33] Skokov, S.; Wheeler, R. A. *Chem. Phys. Lett.* **1997**, *271*, 251–258.

[34] Filatov, M.; Thiel, W. *Chem. Phys. Lett.* **1998**, *295*, 467–474.

[35] Lynch, B. J.; Truhlar, D. G. *J. Phys. Chem. A* **2001**, *105*, 2936–2941.

[36] Johnson, B. G.; Gonzales, C. A.; Gill, P. M. W.; Pople, J. A. *Chem. Phys. Lett.* **1994**, *221*, 100–108.

[37] Koga, N.; Morokuma, K. *Chem. Phys. Lett.* **1985**, *119*, 371–374.

[38] Bearpark, M. J.; Robb, M. A.; Schlegel, H. B. *Chem. Phys. Lett.* **1994**, *223*, 269–374.

[39] Harvey, J. N.; Aschi, M.; Schwarz, H.; Koch, W. *Theor. Chem. Acc.* **1998**, *99*, 95–99.

[40] Siegbahn, P. E. M. In *New Methods in Computational Quantum Mechanics*; Prigogine, I., Rice, S. A., Eds.; Wiley Interscience: New York, 1996; Vol. XCIII of *Advances in Chemical Physics;* pages 333–387.

[41] Siegbahn, P. E. M. *J. Comput. Chem.* **2001**, *22*, 1634–1645.

[42] Bauschlicher, C. W. J.; Partridge, H. *Chem. Phys. Lett.* **1995**, *240*, 533–540.

[43] Hay, P. J.; Wadt, W. R. *J. Chem. Phys.* **1985**, *82*, 299–310.

[44] Li, J.; Schreckenbach, G.; Ziegler, T. *J. Am. Chem. Soc.* **1995**, *117*, 486–494.

[45] van Wüllen, C. *J. Chem. Phys.* **1996**, *105*, 5485–5493.

[46] van Wüllen, C. *Int. J. Quantum Chem.* **1996**, *58*, 147–152.

[47] Gaussian 03, Revision B.05. Frisch, M. J.; Trucks, G. W.; Schlegel, H. B.; Scuseria, G. E.; Robb, M. A.; Cheeseman, J. R.; Montgomery, Jr., J. A.; Vreven, T.; Kudin, K. N.; Burant, J. C.; Millam, J. M.; Iyengar, S. S.; Tomasi, J.; Barone, V.; Mennucci, B.; Cossi, M.; Scalmani, G.; Rega, N.; Petersson, G. A.; Nakatsuji, H.; Hada, M.; Ehara, M.; Toyota, K.; Fukuda, R.; Hasegawa, J.; Ishida, M.; Nakajima, T.; Honda, Y.; Kitao, O.; Nakai, H.; Klene, M.; Li, X.; Knox, J. E.; Hratchian, H. P.; Cross, J. B.; Bakken, V.; Adamo, C.; Jaramillo, J.; Gomperts, R.; Stratmann, R. E.; Yazyev, O.; Austin, A. J.; Cammi, R.; Pomelli, C.; Ochterski, J. W.; Ayala, P. Y.; Morokuma, K.; Voth, G. A.; Salvador, P.; Dannenberg, J. J.; Zakrzewski, V. G.; Dapprich, S.; Daniels, A. D.; Strain, M. C.; Farkas, O.; Malick, D. K.; Rabuck, A. D.; Raghavachari, K.; Foresman, J. B.; Ortiz, J. V.; Cui, Q.; Baboul, A. G.; Clifford, S.; Cioslowski, J.; Stefanov, B. B.; Liu, G.; Liashenko, A.; Piskorz, P.; Komaromi, I.; Martin, R. L.; Fox, D. J.; Keith, T.; Al-Laham, M. A.; Peng, C. Y.; Nanayakkara, A.; Challacombe, M.; Gill, P. M. W.; Johnson, B.; Chen, W.; Wong, M. W.; Gonzalez, C.; Pople, J. A.; Gaussian Inc., Wallingford, CT, **2004**.

[48] Jaguar 5.5, Schrödinger, L. L. C., Portland, OR, 1991–2003.

[49] Tannor, D. J.; Marten, B.; Murphy, R.; Friesner, R. A.; Sitkoff, D.; Nicholls, A.; M., R.; Goddard III, W. A.; Honig, B. *J. Am. Chem. Soc.* **1994**, *116*, 11875–11882.

[50] Qsite, FirstDiscovery Suite v2.0, Schrödinger, L. L. C., Portland, OR, 2002.

[51] Jorgensen, W. L.; Maxwell, D. S.; Tirado-Rives, J. *J. Am. Chem. Soc.* **1996**, *118*, 11225–11236.

[52] Murphy, R. B.; Philipp, D. M.; Friesner, R. A. *Chem. Phys. Lett.* **2000**, *321*, 113–120.

[53] Murphy, R. B.; Philipp, D. M.; Friesner, R. A. *J. Comput. Chem.* **2000**, *21*, 142–1457.

[54] Boese, A. D.; Handy, N. C. *J. Chem. Phys.* **2001**, *114*, 5497–5503.

[55] Gardner, K. A.; Mayer, J. M. *Science* **1995**, *269*, 1849–1851.

[56] Gardner, K. A.; Kuehnert, L. L.; Mayer, J. M. *Inorg. Chem.* **1997**, *36*, 2069–2078.

[57] Bauschlicher, C. W. J.; Ricca, A. In *Recent Advances in Density Functional Methods, Part 2*; Partridge, H., Langhoff, S. R., Eds.; D. P. Chong, World Sci.: Singapore, 1997; pages 165–227.

[58] Rüttinger, W. F.; Ho, D. M.; Dismukes, G. C. *Inorg. Chem.* **1999**, *38*, 1036–1037.

[59] Noodleman, L.; Case, D. A. *Adv. Inorg. Chem.* **1992**, *38*, 423–470.

[60] Perdew, J. P.; A., Z. *Phys. Rev. B* **1981**, *23*, 5048–5079.

[61] Perdew, J. P.; Levy, M. *Phys. Rev. B* **1997**, *56*, 16021–16028.

[62] Zhang, Y.; Yang, W. *J. Chem. Phys.* **1998**, *109*, 2604–2608.

[63] Polo, V.; Kraka, E.; Cremer, D. *Mol. Phys.* **2002**, *100*, 1771–1790.

[64] Lundin, U.; Eriksson, O. *Int. J. Quantum Chem.* **2001**, *81*, 247–252.

[65] Patchkovskii, S.; Autschbach, J.; Ziegler, T. *J. Chem. Phys.* **2001**, *115*, 26–42.

[66] Jaramillo, J.; Scuseria, G. E.; Ernzerhof, M. *J. Chem. Phys.* **2003**, *118*, 1068–1073.

[67] Kümmel, S.; Perdew, J. P. *Mol. Phys.* **2003**, *101*, 1363–1368.

[68] Ciofini, I.; Chermette, H.; Adamo, C. *Chem. Phys. Lett.* **2003**, *380*, 12–20.

[69] Tozer, D. J.; Handy, N. C.; Cohen, A. J. *Chem. Phys. Lett.* **2003**, *382*, 203–210.

[70] Vydrov, O. A.; Scuseria, G. E. *J. Chem. Phys.* **2004**, *121*, 8187–8193.

[71] Bally, T.; Sastry, G. N. *J. Phys. Chem. A* **1997**, *101*, 7923–7925.

[72] Ferreira, K. N.; Iverson, T. M.; Maghlaoui, K.; Barber, J.; Iwata, S. *Science* **2004**, *303*, 1831–1838.

[73] Tommos, C.; Babcock, G. T. *Acc. Chem. Res.* **1998**, *31*, 18–25.

[74] Renger, G. *Biochim. Biophys. Acta* **2001**, *1503*, 210–228.

[75] Siegbahn, P. E. M.; Crabtree, R. H. *J. Am. Chem. Soc.* **1999**, *121*, 117–127.

[76] Siegbahn, P. E. M. *Inorg. Chem.* **2000**, *39*, 2923–2935.

[77] Lind, J.; Shen, X.; Eriksen, T. E.; Merényi, G. *J. Am. Chem. Soc.* **1990**, *112*, 479–482.

[78] Schlodder, E.; Witt, H. T. *J. Biol. Chem.* **1999**, *274*, 30387–30392.

[79] Junge, W.; Haumann, M.; Ahlbrink, R.; Mulkidjanian, A.; Clausen, J. *Philos. Trans. R. Soc. London, Ser. B.* **2002**, *357*, 1407–1418.

[80] Robblee, J. H.; Cinco, R. M.; Yachandra, V. K. *Biochim. Biophys. Acta* **2001**, *1503*, 7–23.

[81] Robblee, J. H.; Messinger, J.; Cinco, R. M.; McFarlane, K. L.; Fernandez, C.; Pizarro, S. A.; Sauer, K.; Yachandra, V. K. *J. Am. Chem. Soc.* **2002**, *124*, 7459–7471.

[82] Cinco, R. M.; McFarlane Holman, K. L.; Robblee, J. H.; Yano, J.; Pizarro, S. A.; Bellacchio, E.; K., S.; Yachandra, V. K. *Biochemistry* **2002**, *41*, 12928–12933.

[83] Haumann, M.; Müller, C.; Liebisch, P.; Iuzzolino, L.; Dittmer, J.; Grabolle, M.; Neisius, T.; Meyer-Klaucke, W.; Dau, H. *Biochemistry* **2005**, *44*, 1894–1908.

[84] Zouni, A.; Witt, H.-T.; Kern, J.; Fromme, P.; Krauss, N.; W., S.; Orth, P. *Nature* **2001**, *409*, 739–743.

[85] Kern, J.; Loll, B.; Luneberg, C.; DiFiore, D.; Biesiadka, J.; D., I. K.; A, Z. *Phys. Chem. Chem. Phys.* **2004**, *6*, 4733–4736.

[86] Kamiya, N.; Shen, J.-R. *Proc. Natl. Acad. Sci. USA* **2003**, *100*, 98–103.

[87] Hasegawa, K.; T.-a., O.; Inoue, Y.; Kusonoki, M. *Chem. Phys. Lett.* **1999**, *300*, 9–19.

[88] Peloquin, J. M.; Campbell, K. A.; Randall, D. W.; Evanchik, M. A.; Pecoraro, V. L.; Armstrong, W. H.; Britt, R. D. *J. Am. Chem. Soc.* **2000**, *122*, 10926–10942.

[89] Hasegawa, K.; Kusonoki, M.; Inoue, Y.; Ono, T.-a. *Biochemistry* **1998**, *37*, 9457–9465.

[90] Dau, H.; Iuzzolino, L.; Dittmer, J. *Biochim. Biophys. Acta* **2001**, *1503*, 24–39.

[91] Chu, H.-A.; Hillier, W.; Debus, R. J. *Biochemistry* **2004**, *43*, 3152–3166.

[92] Liang, W.; Roelofs, T. A.; Cinco, R. A.; Rompel, A.; Latimer, M. J.; Yu, W. O.; Sauer, K.; Klein, M. P.; Yachandra, V. K. *J. Am. Chem. Soc.* **2000**, *122*, 3399–3412.

[93] Hillier, W.; Wydrzynski, T. *Biochemistry* **2000**, *39*, 4399–4405.

[94] Rüttinger, W.; Dismukes, G. C. *Chem. Rev.* **1997**, *97*, 1–24.

[95] Limburg, J.; Vrettos, J. S.; Chen, H.; de Paula, J. C.; Crabtree, R. H.; Brudvig, G. W. *J. Am. Chem. Soc.* **2001**, *123*, 423–430.

[96] Yagi, M.; Narita, K. *J. Am. Chem. Soc.* **2004**, *126*, 8084–8085.

[97] Collins, T. J.; Gordon-Wylie, S. W. *J. Am. Chem. Soc.* **1989**, *111*, 4511–4513.

[98] Collins, T. J.; Powell, R. D.; Slebodnick, C.; Uffelman, E. S. *J. Am. Chem. Soc.* **1990**, *112*, 899–901.

[99] MacDonnel, F. M.; Fackler, N. L. P.; Stern, C.; O'Halloran, T. V. *J. Am. Chem. Soc.* **1994**, *116*, 7431–7432.

[100] Smith, K. M.; Poli, R.; Harvey, J. N. *Chem. Eur. J.* **2001**, *7*, 1679–1690.

[101] Hess, J. S.; Leelasubcharoen, S.; Rheingold, A. L.; Doren, D. J.; Theopold, K. H. *J. Am. Chem. Soc.* **2002**, *124*, 2454–2455.

[102] Jensen, V. R.; Poli, R. *J. Phys. Chem. A* **2003**, *107*, 1424–1432.

[103] Harvey, J. N.; Poli, R.; Smith, K. M. *Coord. Chem. Rev.* **2003**, *238–239*, 347–361.

[104] Carreón-Macedo, J.-L.; Harvey, J. N. *J. Am. Chem. Soc.* **2004**, *126*, 5789–5797.

[105] Sjödin, M.; Styring, S.; Åkermark, B.; Sun, L.; Hammarström, L. *J. Am. Chem. Soc.* **2000**, *122*, 3932–3936.

[106] Demadis, K. D.; Hartshorn, C. M.; Meyer, T. J. *Chem. Rev.* **2001**, *101*, 2655–2685.

[107] Braun-Sand, S. B.; Wiest, O. *J. Phys. Chem. A* **2003**, *107*, 285–291.

[108] Siegbahn, P. E. M. *Theor. Chem. Acc.* **2001**, *105*, 197–206.

[109] Marcus, R. A. *J. Chem. Phys.* **1965**, *43*, 679–701.

[110] Marcus, R. A. *Rev. Mod. Phys.* **1993**, *65*, 599–610.

[111] Creutz, C. *Prog. Inorg. Chem.* **1983**, *30*, 1–73.

[112] Broo, A.; Larsson, S. *Chem. Phys.* **1992**, *161*, 363–378.

[113] Ferretti, A.; Lami, A.; Villani, G. *Inorg. Chem.* **1998**, *37*, 2799–2805.

[114] Bencini, A.; Ciofini, I.; Daul, C. A.; Ferretti, A. *J. Am. Chem. Soc.* **1999**, *121*, 11418–11424.

[115] Vollmer, E.; Kordel, M.; Koslowski, T. *Z. Phys. Chem.* **2004**, *218*, 611–622.

[116] Ruiz, E.; Salahub, D. R.; Vela, A. *J. Phys. Chem.* **1996**, *100*, 12265–12276.

[117] Radzicka, A.; Wolfenden, R. *Science* **1995**, *267*, 90–92.

[118] Warshel, A.; Strâjbl, M.; Villà, J.; Florián, J. *Biochemistry* **2000**, *39*, 14728–14738.

[119] Appleby, T. C.; Kinsland, C.; Begley, T. P.; E., E. S. *Proc. Natl. Acad. Sci. USA* **2000**, *97*, 2005–2010.

[120] Miller, B. G.; Hassel, A. M.; Wolfenden, R.; Milburn, M. V.; Short, S. A. *Proc. Natl. Acad. Sci. USA* **2000**, *97*, 2011–2016.

[121] Wu, N.; Mo, Y.; Gao, J.; Pai, E. F. *Proc. Natl. Acad. Sci. USA* **2000**, *97*, 2017–2022.

[122] Harris, P.; Poulsen, J.-C. N.; Jensen, K. F.; Larsen, S. *Biochemistry* **2000**, *39*, 4217–4224.

[123] Miller, B. G.; Snider, M. J.; Wolfenden, R.; Short, S. A. *J. Biol. Chem.* **2001**, *276*, 15174–15176.

[124] Raugei, S.; Cascella, M.; Carloni, P. *J. Am. Chem. Soc.* **2004**, *126*, 15730–15737.

[125] Singleton, D. A.; Merrigan, S. R.; Kim, B. J.; Beak, P.; Phillips, L. M.; Lee, J. K. *J. Am. Chem. Soc.* **2000**, *122*, 3296–3300.

Acknowledgments

It is with great pleasure that I acknowledge the persons who have assisted me through the years. My supervisors Margareta and Per have been simply wonderful in their support of me in times of trouble. Without their help and understanding, I would never have reached this page.

When it comes to the thesis, I thank my co-author Tomek whose amiability and careful research attitude make him a great colleague. Also on the limited list of co-authors is Arianna whose excellence always has been a guideline to me. I am particularly grateful to Björn Atldax for his illustrations of highly photosynthetic plants and to Daniel Blå for his professional support in designing the layout.

Mattias is the greatest coach and roommate I will ever have and he has solved many of my problems as they appeared, and thanks to Ella for nice conversations on the phone. The atmosphere in the group has been most accommodating and I acknowledge all former and present members in chronological order: Maria, Fahmi, Rajeev, Kyung–Bin, Vladimir, Dimos, Micke, Fredrik, Mattias, Arianna, Dan, Tomek, Sven, Johannes, Valentin, Dimitri, and finally Tomas who hopefully continues the photosynthesis path. There are also some closely connected people I would like to highlight: Matteo for his heart of gold, Simone for the hospitality of him and his wife, and Oscar simply for being himself. Thank you Britta for the flowers!

To the important people in my life that have not been directly involved in the thesis, I hope I can show my appreciation in many other ways.